# Low-temperature alteration of monazite: Fluid mediated coupled dissolution-precipitation, irradiation damage, and disturbance of the U-Pb and Th-Pb chronometers

Anne-Magali Seydoux-Guillaume, Jean-Marc Montel, Bernard Bingen, Valérie Bosse, Philippe de Parseval, Jean-Louis Paquette, Emilie Janots, Richard Wirth

# Low-temperature alteration of monazite: Fluid mediated coupled dissolution–precipitation, irradiation damage, and disturbance of the U–Pb and Th–Pb chronometers

Anne-Magali Seydoux-Guillaume [a,*], Jean-Marc Montel [b], Bernard Bingen [c], Valérie Bosse [d], Philippe de Parseval [a], Jean-Louis Paquette [d], Emilie Janots [e], Richard Wirth [f]

[a] GET, UMR 5563 CNRS, Université Paul Sabatier, IRD, 14 avenue Edouard Belin, 31400 Toulouse, France
[b] G2R, CNRS, Ecole Nationale Supérieure de Géologie, Nancy-Université, BP 70239, 54056 Vandoeuvre-les-Nancy, France
[c] Geological Survey of Norway, 7491 Trondheim, Norway
[d] Clermont Université, CNRS UMR 6524, Université Blaise Pascal and IRD, 5 rue Kessler, 63038 Clermont-Ferrand France
[e] ISTerre BP 53, 38041 Grenoble CEDEX 9, France
[f] Helmholtz-Zentrum Potsdam, Deutsches GeoForschungsZentrum, Telegrafenberg, D-14473 Potsdam, Germany

Low-temperature alteration of monazite is documented in three centimeter-sized monazite crystals from Norway (Arendal), Madagascar (Ambato), and Sri Lanka. The three crystals have different chemical compositions, especially in their U, Th, Y and Pb contents and have $^{208}Pb/^{232}Th$ ages ranging from 491 to 900 Ma. Optical microscope (OM), Scanning Electron Microscope (SEM) and Transmission Electron Microscope (TEM) images and electron microprobe analyses (EPMA) show that all three preserve a similar patchy texture. This texture is interpreted as resulting from an alteration reaction in which unaltered monazite (Mnz1) reacts to form a secondary, Th–U(Y)-depleted, high-Th/U, monazite (Mnz2) accompanied by thorite/huttonite ($ThSiO_4$), thorianite ($ThO_2$) and xenotime ($YPO_4$), the proportions of which are dependent upon the initial composition of the monazite (Mnz1). Images reveal variably intense internal fracturing, with cracks filled with Th-rich ± Fe-rich phases. Monazite-xenotime thermometry demonstrates that the pristine monazites (Mnz1) interacted with a low-temperature fluid. The alteration process is interpreted to follow a mechanism of fluid-mediated coupled dissolution–precipitation. Chemical dating with the electron microprobe shows no Th–U–Pb age differences between primary and secondary monazites, except in the case of the Ambato monazite, in which altered domains yield older (750 Ma) apparent ages than the pristine Mnz1 domains. U–Pb and Th–Pb isotope dating using LA-ICP-MS yields ages consistent with electron probe dates for pristine Mnz1 zones. However, disturbance of these systems in the altered monazite domains leads to variable age results for these, depending on sample. In the case of Sri Lanka and Arendal, only $^{208}Pb/^{232}Th$ dates provide a reasonable estimate of the age of alteration, which are constrained to be 450 and 864 Ma, respectively. U/Pb systems are disturbed due to common Pb contamination (up to 40%) and U fractionation relative to Th during alteration, responsible for depletion of U in altered monazites (and increase of Th/U). In contrast, for the Ambato monazite, both the U–Pb and Th–Pb systems were affected and yield inconsistent older dates for altered zones. This is attributed to significant common Pb contamination (up to 80%), which affects all Pb isotopes and explains why electron probe ages are erroneous. Th–U-silicate contamination during measurement, resulting from the presence of a numerous nano-phases and nano-fractures filled with Th–U-silicates that are visible only under TEM, also contributes to the anomalously old ages for these disturbed (Mnz2) domains. These results demonstrate the important role of radiation damage effects, in particular swelling-induced fracturing, and the essential role of porosity and cracks, which allow fluid (charged with elements) migration through monazite during low-temperature alteration.

## 1. Introduction

The Light Rare Earth Element (LREE) orthophosphate monazite is a common accessory mineral in both metamorphic (see review in Spear and Pyle, 2002) and magmatic rocks. Because of its high Th content and to a lesser extent U and low content of common Pb, monazite plays an important role as a U–Th–Pb geochronometer (Parrish, 1990; Harrison et al., 2002).

Monazite is highly resistant to alteration, as shown by its widespread occurrence as detrital mineral in sands and sandstones (Van Emden et al., 1997; Roy, 1999). However, some highly aggressive fluids may

* Corresponding author.
*E-mail address:* anne-magali.seydoux@get.obs-mip.fr (A.-M. Seydoux-Guillaume).

partially or totally alter monazite in rocks, even at moderate temperature. For example, Poitrasson et al. (1996, 2000) show that monazite is significantly altered in granitic rocks at 200–300 °C during sericitization, greisenization or chloritization. Cuney and Mathieu (2000), Hecht and Cuney (2000) and Mathieu et al. (2001) have shown that monazite is destroyed by low-T, highly saline brines in the vicinity of uranium deposits. Other studies have shown that monazite can be altered or broken down by fluorine or $CO_2$-rich fluids, producing allanite, apatite, rhabdophane, thorianite, thorite/huttonite, bastnäesite, or synchysite (Finger et al., 1998; Berger et al., 2008; Bosse et al., 2009; Budzyn et al., 2010; Didier et al., 2011; Janots et al., 2011; Janots et al., 2012).

The stability of monazite in fluids has been also investigated experimentally. The solubility and kinetics of dissolution of natural monazite (Oelkers and Poitrasson, 2002; Schmidt et al., 2007) or synthetic end-members ($LaPO_4$—Schmidt et al., 2007, $NdPO_4$—Devidal et al., 1998; Poitrasson et al., 2004; Pourtier et al., 2010; $CePO_4$—Tropper et al., 2011) have been determined in $H_2O$–NaCl–HCl fluids. These studies indicate both low solubility and kinetics in pure water, and enhanced solubility and kinetics in highly acidic or alkaline solutions such as brines. A second type of experiment has addressed the resetting mechanism(s) of geochronological systems (U–Pb and Th–Pb) in monazite in the presence of fluids (Teufel and Heinrich, 1997; Seydoux-Guillaume et al., 2002a; Williams et al., 2011). These studies demonstrate that coupled dissolution–precipitation is more effective than solid-state volume diffusion (Cherniak et al., 2004; Gardés et al., 2006, 2007; Cherniak, 2010) in the resetting of geochronological systems in monazite, especially in the presence of fluids enriched in alkalies. Finally, various experiments have considered the alteration mechanism of natural monazite (mineral stability and element mobility) in the presence of fluid of various compositions and at various temperature conditions (Seydoux-Guillaume et al., 2002a; Hetherington et al., 2010; Harlov et al., 2011). All these experiments confirm that monazite is indeed altered by alkaline fluids through a coupled dissolution–precipitation mechanism.

However, up to now, no experimental work has been able to reproduce the classic internal textures observed in many monazites in pegmatites (Brazil—Bilal et al., 1998; Norway—Seydoux-Guillaume et al., 2007; xenotime and monazite from Norway—Hetherington and Harlov, 2008; Norway—Nasdala et al., 2010). The chemical and isotopic characterization and analysis of these textures will form the focus of the present study. Despite originating from different localities, and having different ages and chemical compositions, all the selected monazite samples present similar textural relationships characterized by close co-occurrence of monazite, partially (Bilal et al., 1998; Seydoux-Guillaume et al., 2007; Hetherington and Harlov, 2008) or completely (Nasdala et al., 2010) altered, with a Th-rich phase such as thorianite ($ThO_2$; Thn) or thorite/huttonite ($ThSiO_4$; Thr/Htn). To our knowledge, the only experimental work that has successfully produced a Th-rich phase as the result of monazite alteration is that of Seydoux-Guillaume et al. (2002a). In those experiments, thorianite crystallized between 800 and 1200 °C in the presence of pure $H_2O$.

The present study investigates large (cm) monazite single crystals from three distinct pegmatite localities in Norway, Madagascar, and Sri Lanka. The crystals share a microtexture characterized by the presence of pristine monazite (Mnz1) partly altered into secondary monazite (Mnz2) accompanied by a Th-rich phase (Th-silicate or Th-oxide), and locally xenotime (Xnt). The samples are characterized using optical microscopy, back scattered electron imaging (BSE), electron probe microanalysis (EPMA) and transmission electron microscope (TEM). The preserved age characteristics have been investigated by chemical dating using EPMA and isotopic dating using laser ablation inductively coupled plasma-mass spectrometry (LA-ICP-MS). Comparison of the results obtained by these very different techniques is highly illuminating because they are complementary: high spatial resolution (max. 5 $\mu m^3$ for the volume analyzed) but lower precision total Pb chemical dating with EPMA, as against higher accuracy but lower spatial resolution (50 $\mu m^3$ for the volume analyzed) for isotopic dating using LA-ICP-MS. The Arendal sample was previously studied by Seydoux-Guillaume et al. (2007). Here we focus on the chemical and mineralogical changes, during fluid–rock interactions and on its geochronological effects.

## 2. Analytical methods

### *2.1. Scanning Electron Microscope (SEM), Electron Microprobe Analysis (EPMA) and chemical dating*

Qualitative analysis and mapping using Electron Dispersive X-ray Spectroscopy (EDX) and Back Scattered Electron (BSE) images were performed using the JEOL 6360 equipped with a Sahara detector from PGT at the GET (Géosciences Environnement Toulouse) in Toulouse (France) (Janots et al., 2009).

Quantitative analysis was performed at GET using a CAMECA SX50 EPMA operating with the SAM-X system. Major and minor elements were measured with 20 nA probe current and 15 kV accelerating voltage using following standards: periclase (Mg), wollastonite (Ca and Si), pyrophanite (Mn and Ti), corundum (Al), haematite (Fe), baryte (Ba), albite (Na), sanidine (K), chromite (Cr), zircon (Hf and Zr), graftonite (P), $UO_2$ (U), $ThO_2$ (Th), and experimentally synthesised $Pb_2P_2O_7$ (Pb), $REEPO_4$ and $YPO_4$.

All EMPA dating was carried out at GET in Toulouse using a CAMECA SX50 EPMA operating with the SAM-X system. Pb and REE standards are in-house synthetic phosphates. U, Th, and Pb were measured with 300 nA probe current and 15 kV accelerating voltage. With these conditions, the analyzed area is about 1.5 μm diameter according to the equation of Castaing (1960). Thorium was measured using the Mα line, with $ThO_2$ as a standard, and 30 s count time on peak and background. Uranium was measured on the Mβ line, with synthetic $UO_2$ as standard, 90 s count time on peak and 60 s on background. Pb was measured using the Mβ line, with $Pb_2P_2O_7$ as a standard, 150 s count time on peak and 100 s on background. The three elements were counted using PET crystals, U and Th being counted on one spectrometer while Pb was counted simultaneously on another spectrometer. Other analytical details addressing the issues described in Jercinovic and Williams (1999) can be found in Montel et al. (2011). With these operating conditions, typical uncertainties are due to counting statistics (Ancey et al., 1978) and are ± 350 ppm, ± 250 ppm, ± 900 ppm for Pb, U, and Th respectively. Uncertainties on Pb, U, and Th are estimated individually for each analysis, then ages are calculated for each measurement (Montel et al., 1996) and the 2σ standard deviation (95% confidence interval) is calculated by propagation of errors using Monte-Carlo simulation.

### *2.2. Laser ablation-inductively coupled plasma-mass spectrometry (LA-ICP-MS): instrumentation and analytical method*

U–Th–Pb isotopic analysis of monazite was conducted by laser ablation inductively coupled plasma spectrometry (LA-ICP-MS) at the Laboratoire Magmas et Volcans, Clermont-Ferrand (France). Analysis involved ablation with a Resonetics Resolution M-50 powered by an ultra short pulse (<4 ns) ATL Atlex Excimer laser system operating at a wavelength of 193 nm (detailed description in Müller et al., 2009). A spot diameter of 7 μm associated with repetition rates of 1 Hz and laser energy of 6 mJ producing a fluence of 12 $J/cm^2$ was used for monazite dating. The ablated material is carried into a helium stream, and then mixed with nitrogen and argon, before injection into the plasma source of an Agilent 7500 cs ICP-MS equipped with a dual pumping system to enhance the sensitivity.

Alignment of the instrument and mass calibration were performed before every analytical session using the NIST SRM 612 reference glass, through inspection of the $^{238}U$ signal and minimizing the $ThO^+/Th^+$ ratio ($\ll 1\%$). The mean sensitivity for $^{238}U$ using a spot size of 44 μm is about 15,000–20,000 cps/ppm. The analytical method for isotope dating of monazite with laser ablation ICPMS is similar to that

developed for zircon and monazite as reported in Tiepolo (2003) and Paquette and Tiepolo (2007). The signals for $^{204}$(Pb + Hg), $^{206}$Pb, $^{207}$Pb, $^{208}$Pb, $^{232}$Th and $^{238}$U masses were acquired. The occurrence of common Pb in the sample can be monitored by the evolution of the $^{204}$(Pb + Hg) signal intensity, but no common Pb correction was applied owing to the large isobaric interference from Hg. The $^{235}$U signal is calculated from $^{238}$U on the basis of the ratio $^{238}$U/$^{235}$U = 137.88. Single analyses consisted of 30 s of background integration with laser-off followed by 1 min integration with the laser firing and a 30 seconds delay to wash out the previous sample (approximately 10 s for 6 orders of magnitude) and prepare for the analysis.

Data were corrected for U–Pb fractionation occurring during laser sampling and for instrumental mass discrimination (mass bias) by standard bracketing with repeated measurements of the Moacyr monazite standard (Gasquet et al., 2010). At the beginning and end of every run, repeated analyses of the Manangotry monazite (Paquette and Tiepolo, 2007), treated as an unknown, were used to independently control the reproducibility and accuracy of the corrections applied. Data reduction was carried out with the software package GLITTER® (Macquarie Research Ltd., 2001—van Achterbergh et al., 2001; Jackson et al., 2004). For each analysis, the time-resolved signals of single isotopes and isotope ratios were monitored and carefully inspected to monitor the presence of perturbations related to inclusions, fractures, mixing of different age domains or common Pb. Calculated ratios were exported from GLITTER® and Concordia ages and diagrams generated using the Isoplot/Ex v. 2.49 software package (Ludwig, 2001). The concentrations of U–Th–Pb were calibrated relative to the certified contents of Moacyr monazite standard (Seydoux-Guillaume et al., 2002b, 2004).

### *2.3. Transmission Electron Microscope (TEM) coupled with Focused-Ion-Beam (FIB) preparation*

This technique was used in order to characterize the structural state of monazite in contact with thorite. The Arendal monazite was previously studied by Seydoux-Guillaume et al. (2007) and new TEM foils were prepared from the Ambato monazite to complete these observations. The Focused-Ion-Beam (FIB) method (Overwijk et al., 1993; Young, 1997; Roberts et al., 2001; Seydoux-Guillaume et al., 2003; Wirth, 2004, 2009) allows cutting site-specific TEM foils, ~15–20 μm by 10–15 μm, and ~100 nm thick. Milling was done using gallium ions accelerated to 30 keV. The TEM foil was cut perpendicular to the surface of the sample, and so provided information with respect to the depth from the surface of the specimen. The site-specific specimens were prepared with the FEI FIB200 instrument at the GeoForschungsZentrum (GFZ)—Potsdam. Transmission Electron Microscope (TEM) studies were carried out with the Philips CM200 TEM at the GFZ—Potsdam, operating at 200 keV, and equipped with an energy-dispersive X-ray analyzer (EDX) with ultra-thin window, and a $LaB_6$ filament.

## 3. Sample descriptions: hand specimen and transmitted light

Three large (several centimeters in diameter) monazite monocrystals were used. A piece of each was prepared for microscopic studies (optical, SEM and EPMA, ±TEM). The first crystal is from an unknown locality in Sri Lanka and was donated by T. Geisler (Univ. Bonn). It is the least altered of the three monazites studied. It shows a relatively homogeneous yellow color, and cracks traverse the entire crystal but are more concentrated in some parts of the grain (Fig. 1a). The two other crystals were provided by Benjamin Rondot, from Muséum National d'Histoire Naturelle. The sample named "Ambato" is from Ambatofotsikely in Madagascar. This crystal is mostly yellow in color but has several areas preserving a reddish color, generally associated with alteration. In thin section (Fig. 1b) a large part of the Ambato crystal is dark in color, corresponding to the altered zones, with cracks sometimes filled with reddish inclusions (iron oxides).

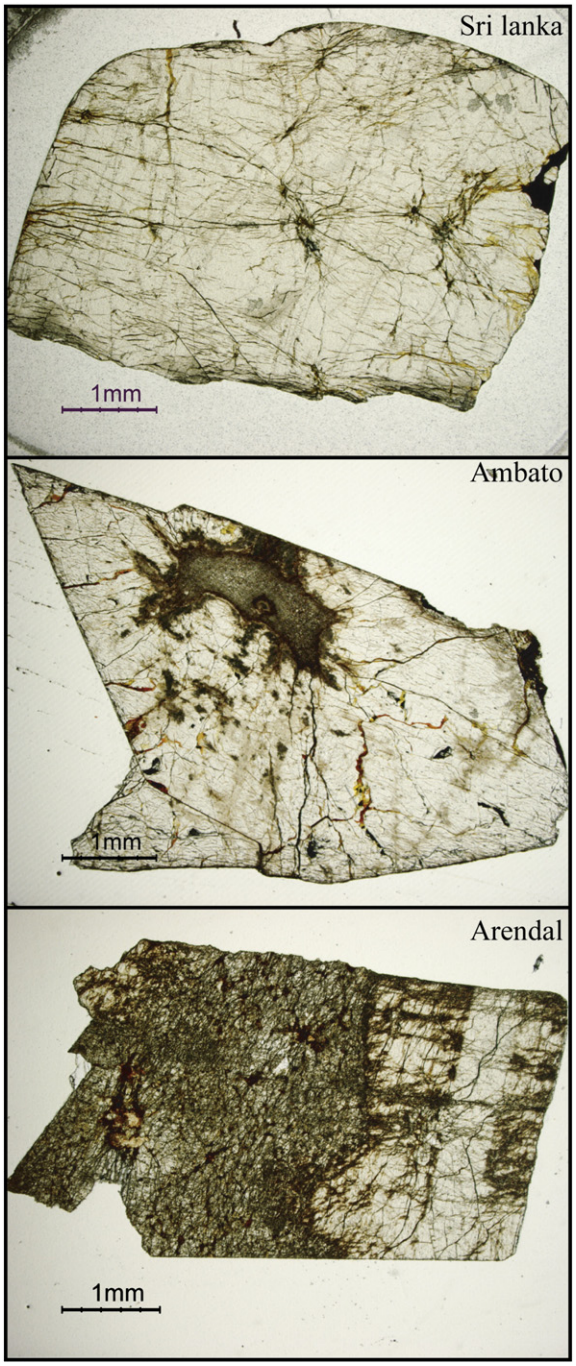


**Fig. 1.** Transmitted light binocular microscope photo of three thin sections of large monazite single crystals from three localities in Sri Lanka, Madagascar and south-Norway. The alteration features are more penetratively developed from Sri Lanka to the Ambato and the Arendal samples.

The third monazite crystal, is denoted as "Arendal", as it comes from this pegmatite district and was previously studied in detail by Seydoux-Guillaume et al. (2007). Geochronological data obtained in this study suggests that the sample is from Iveland-Evje pegmatite field in Agder. It is a reddish-brown, dull and opaque crystal. Optical observations (Fig. 1c) show that the crystal is pervaded by cracks that are always filled with orange to red inclusions (iron oxides).

## 4. Sample descriptions: from micrometer to nanometer

Back scattered electron (BSE) images coupled with energy dispersive X-ray (EDX) mapping (Figs. 2 to 4) show that the crystals contain

thorianite or thorite (we will use thorite to denote the thorium silicate, although it could be huttonite) and sometimes xenotime inclusions.

*4.1. Sri Lanka monazite (Fig. 2)*

For the most part, the crystal appears uniformly gray in BSE, suggesting that it is chemically homogeneous (Mnz1). Some parts of the crystal are traversed by an interconnected network of fractures, several mm-long (Fig. 2c). A monazite that is darker in BSE (Mnz2—Fig. 2d) is systematically developed as zones or halos that are concentric around thorite or thorianite inclusions. Chemical mapping (Fig. 2a) demonstrates that this darker monazite is depleted in Th and Si and enriched in Ce and P. Cracks around thorianite are radial and intersect both Mnz2 and Mnz1 (Fig. 2b), suggesting that fracturing is directly related to the presence of this Th-rich phase and took place after the formation of both Mnz1 and Mnz2. Some porosity occurs in the vicinity of thorianite (e.g. black zones in Fig. 2b and d). The preliminary interpretation from this textural evidence is that the initial higher-Th Mnz1 transformed to the assemblage Mnz2 + thorite/thorianite + quartz (Fig. 2—Si map), and that the formation of the Th-rich minerals during this transformation is responsible for later fracturing.

*4.2. Ambato monazite (Fig. 3)*

The Ambato crystal contains larger areas affected by fracturing and the alteration of Mnz1 to Mnz2 and Th-phases (several mm in Fig. 3c). Xenotime (Xnt, Fig. 3a) is observed together with Mnz2 and thorite. Th-rich phases occur both as isolated large crystals (up to 100 μm), and dispersed smaller grains (Figure 3a, b and d). Porosity and intense fracturing are observed in all altered domains (e.g. Fig. 3d). There are two varieties of fractures: radial fractures around Th-rich phases, which propagate through the Mnz2 phase (Fig. 3b), and extended fractures that traverse across the entire crystal (Fig. 1b). Segments of the latter fractures affect only the unaltered parts of the crystal and terminate in the vicinity of the altered zones (e.g. see the fractures stopping just before the large Th-rich inclusion Fig. 3a or Fig. 3c).

*4.3. Arendal monazite (Fig. 4)*

Only a small amount of the initial monazite Mnz1 is preserved in this crystal (right zone in Fig. 1c and middle zone in Fig. 4b). Thorite (up to 100 μm in size) and xenotime crystals larger than 100 μm (Fig. 4b, c and d) can be observed in the altered zones (Fig. 4a). Two kinds of fractures dominate the crystal: radial cracks around thorites, as seen in Fig. 4c and d, and a dense network of fractures that occur throughout the entire crystal without apparent preferential orientation (Fig. 4b). Fractures are in filled by a Th-rich phase (Fig. 4a and d).

*4.4. Observations at nanometer scale using Transmission Electron Microscope (TEM) (Fig. 5)*

Two TEM foils were prepared, across the contact between the thorite (Thr) and altered monazite (Mnz2) in both the Arendal and Ambato crystals. Detailed results concerning the structural state of the Arendal crystal have been reported previously (Seydoux-Guillaume et al., 2007). However a new bright field (BF) image is presented in Fig. 5a

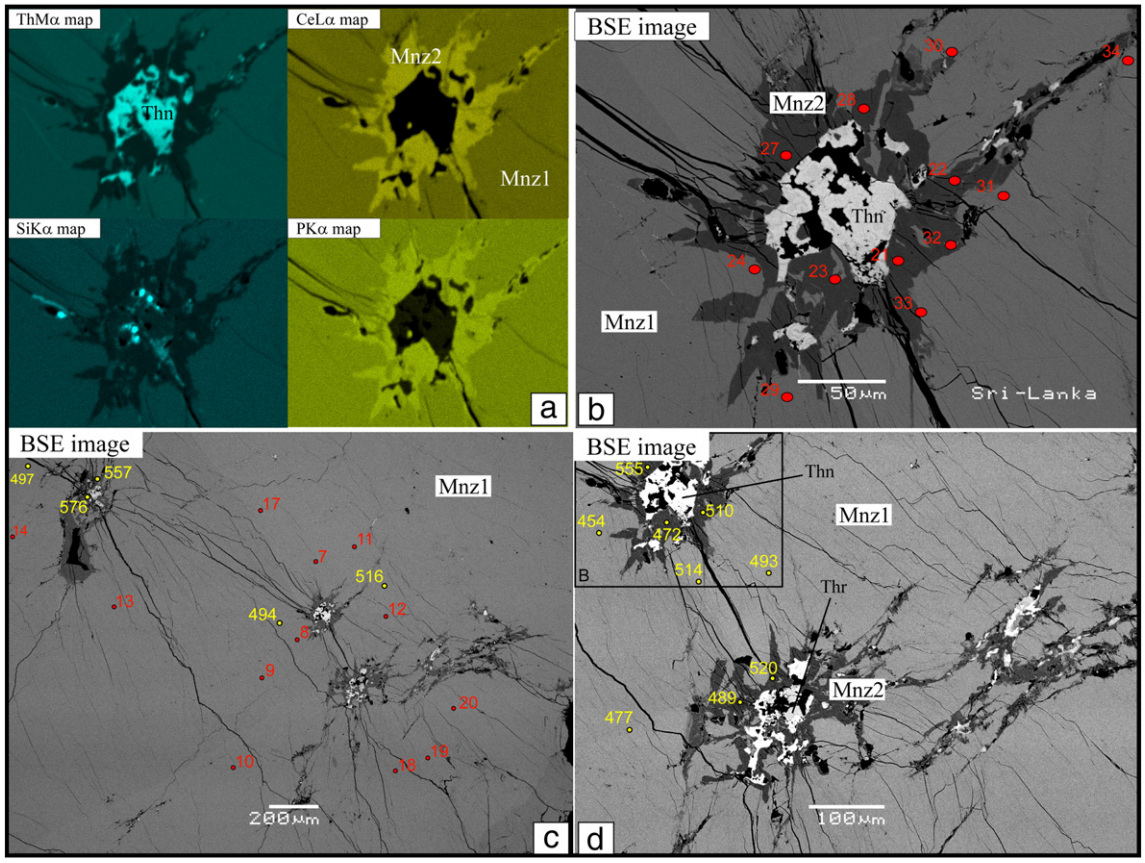


**Fig. 2.** Th, Si, Ce, P-chemical composition maps (a) and Back Scattered Electron (BSE) images (b–d) of a selected area of the Sri-Lanka monazite sample. The large monazite single crystal is composed of pristine monazite (Mnz1) and localized alteration zones, consisting of Th-depleted monazite (Mnz2) associated with Th-rich phase thorianite and/or thorite (Thn/Thr). Altered zones are connected to each other by a dense fracturing network across the entire crystal. Red ellipses correspond to location of LA-ICP-MS analyses with # numbers and yellow ellipses to EPMA chemical ages.

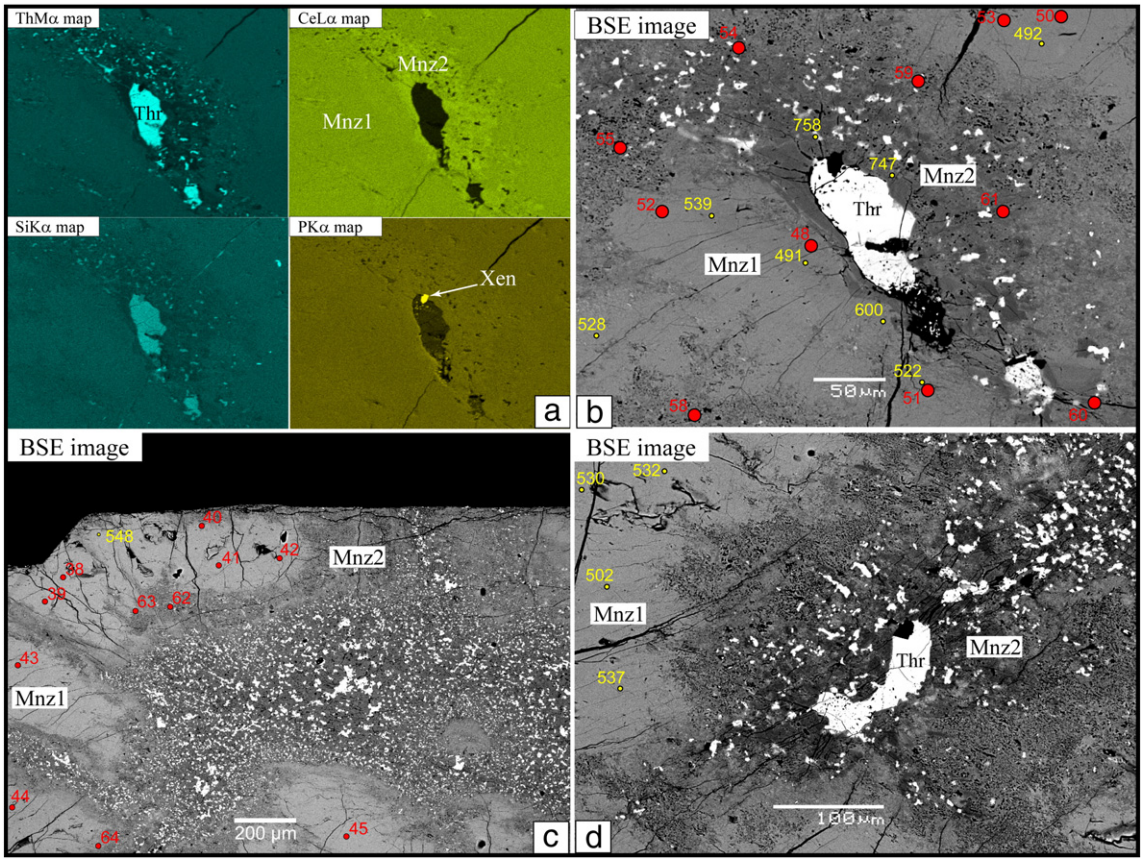


**Fig. 3.** Th, Si, Ce, P-chemical composition maps (a) and BSE images (b–d) of the Ambato monazite sample. The same features as in Fig. 2 are shown.

to provide a comparison with the Ambato monazite. Both altered monazites (Mnz2, Fig. 5a and b) show the characteristic mottled diffraction contrasts, indicating limited lattice distortion and radiation damage (Seydoux-Guillaume et al., 2002c, 2003, 2004, 2007), even along the thorite–monazite interface (Fig. 5c and e; Seydoux-Guillaume et al., 2007). In contrast, the thorite is totally amorphous (absence of diffraction contrasts for Thr—Fig. 5e). In accordance with the observations based on SEM images (Fig. 3), the TEM images show that the Ambato monazite is traversed by cracks originating along the thorite–monazite interface, propagating through Mnz2 and filled with amorphous thorite (Thr in Fig. 5e). Even when in direct contact with these cracks, monazite is crystalline and has the same mottled diffraction contrasts that can be seen in Fig. 5b. Mnz2 contains inclusions of polycrystalline hematite (Hmt—Fig. 5d) infilling large pockets (2–3 µm in diameter) completely included in Mnz2 or infilling cracks (Fig. 5c and e).

## 5. Chemical composition: EPMA

The average compositions of the different phases (Mnz1 and 2, Xnt, and Thr) are given in Tables 1 and 2. Fig. 6 presents element composition spectra for Mnz2 normalized against Mnz1 in order to show the chemical changes associated with alteration. These chemical changes are also visualized in the binary plot of Fig. 7.

### 5.1. Sri Lanka monazite

Mnz1 is very rich in Th (~23 wt.% $ThO_2$) and has associated high $SiO_2$ contents (~5 wt.%); Pb, Ca, Y, MREE (Dy) and U oxides are less than 1 wt.%, LREE (La–Gd) concentrations are ~48 wt.% and $P_2O_5$ ~22 wt.% (Table 1). Mnz2 is strongly depleted in Th (~5 wt.% $ThO_2$), $SiO_2$ (~0.65 wt.%) and $UO_2$ (~0.09 wt.%, Fig. 6).As a result, Mnz2 is enriched in $LREE_2O_3$ (~63 wt.%) and $P_2O_5$ (28 wt.%). The Th/U ratio increases from 30 for Mnz1 to 64 for Mnz2. Thr and Thn display low EPMA totals (~90 wt.%), and contain few measurable cations other than (Th, U) and Si. Only the Fe concentration is occasionally high (up to 7 wt.% in Thr), but it is difficult to be certain that the Fe is actually incorporated into the Thr structure rather than present as a mineral inclusion in Thr. $UO_2$ is higher in Thr (~2 wt.%$UO_2$) than in thorianite (ca 0.7 wt.% $UO_2$).

The distribution of the data is visible in the binary compositional diagram (REE + Y + P) vs (Th + U + Si) of Fig. 7a; Mnz1 analyses plot along a line between Mnz2, which lies near an end member depleted in Th and a Th-rich phase depleted in REE and P.

### 5.2. Ambato monazite

Ambato Mnz1 is characterized by high $ThO_2$ (~14 wt.%) associated with relatively high $SiO_2$ (~3 wt.%); Pb, Ca, MREE (Dy) and $UO_2$ are less than 1 wt.%, and $Y_2O_3$ is near 1 wt.%. In comparison with Mnz1, Mnz2 is depleted in $ThO_2$ (~6 wt.%), $SiO_2$ (~1.15 wt.%), $Y_2O_3$ (0.61 wt.%) and $UO_2$ (~0.08 wt.%, Fig. 6). The Th/U ratio increases from 25 for Mnz1 to 71 for Mnz2. Thorite, which has a low EPMA total, is composed essentially of $ThO_2$ (72 wt.%), $SiO_2$ (~9 wt.%) and $UO_2$ (~2.6 wt.%), resulting in a Th/U ratio of 28. Xenotime has high $Y_2O_3$ (50 wt.%), $P_2O_5$ (~37 wt.%), $Gd_2O_3$ (~6 wt.%) and $HREE_2O_3$ (8 wt.%), but contains only very low amounts of $ThO_2$ (~0.22 wt.%), and PbO (~0.08 wt.%). U is below the detection limit (Table 2). Both monazite types (Mnz1 and Mnz2) plot along a straight line in the compositional diagram (REE + Y + P) vs (Th + U + Si), with xenotime and thorite at the ends of that line (Fig. 7b).

### 5.3. Arendal monazite

Mnz1 is initially heterogeneous in composition, with the variations interpreted as reflecting relict magmatic zoning (Mnz1 vs Mnz1′—sharp

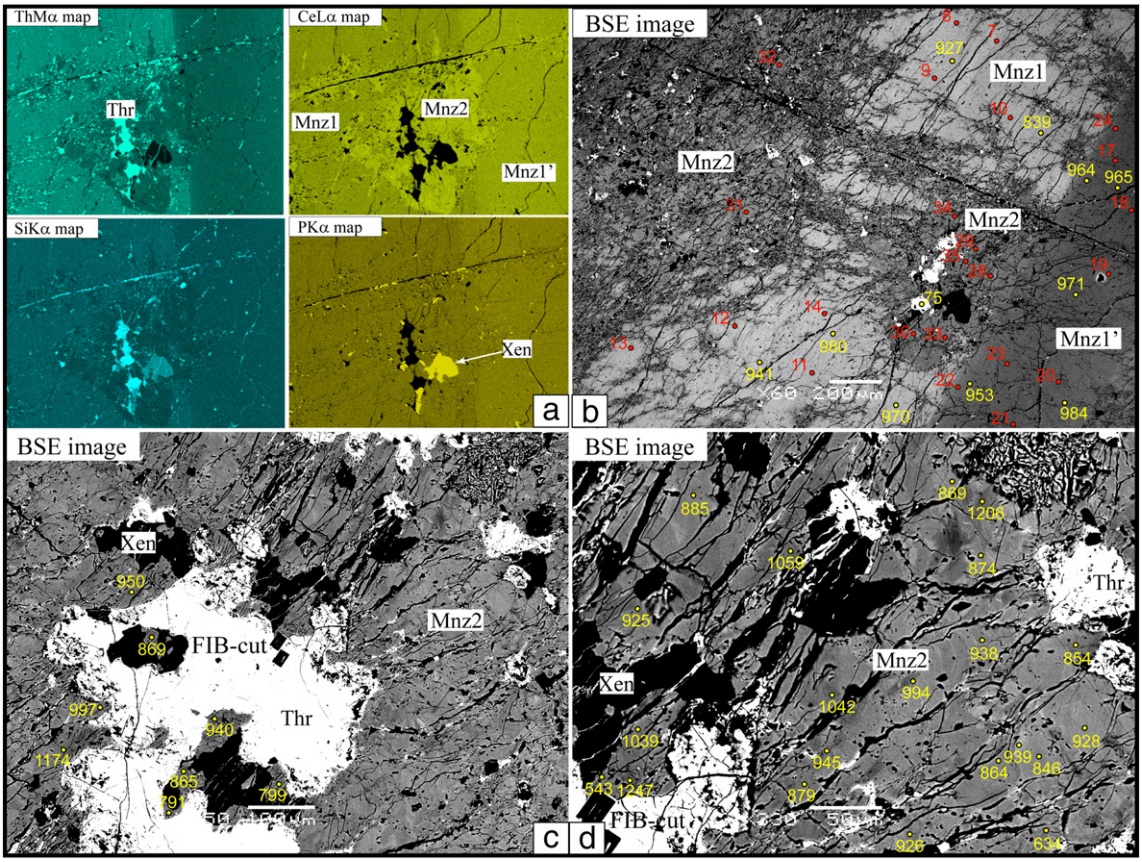


**Fig. 4.** Th, Si, Ce, P-chemical composition maps (a) and BSE images (b–d) of the Arendal monazite sample. The same features as in Fig. 2 are shown. Note that the pristine monazite can be divided into two magmatic zones Mnz1 and Mnz1′. Dense fracturing network crosscuts the entire crystal and originates at the Th-silicate boundary.

interface Fig. 4B): the main variation is in the Th content (12 % $ThO_2$ to 7 % $ThO_2$; Table 1). Mnz2 is depleted in $ThO_2$ (~6 wt.%), $SiO_2$ (~0.66 wt.%), $Y_2O_3$ (0.48 wt.%) and $UO_2$ (~0.13 wt.%, Table 2) with respect to both Mnz1 and Mnz1′. These changes are illustrated using the plot of Mnz2 normalized against Mnz1 and Mnz1′ for the main elements (Fig. 6). The Th/U ratio increases from 18 (Mnz1) and 11 (Mnz1′) for unaltered monazite, to 48 for altered monazite (Mnz2). Thorite, which has low EPMA totals, is composed essentially of $ThO_2$ (63 wt.%), $SiO_2$ (~16 wt.%) and $UO_2$ (~7 wt.%), resulting in a Th/U ratio of 9. Xenotime has high $Y_2O_3$ (45 wt.%) with $P_2O_5$ (~35 wt.%), $Gd_2O_3$ (~6 wt.%) and $HREE_2O_3$ (8 wt.%), but contains very low $ThO_2$ (~0.87 wt.%), PbO (~0.08 wt.%), and $UO_2$ (~0.29 wt.%, Table 2).

These compositional variations result in a distribution of monazite analyses (1, 1′ and 2) along a straight line in the compositional diagram (REE + Y + P) vs (Th + U + Si) (Fig. 7c), with Xnt and Thr at the extremities of the line.

### 5.4. Estimation of the temperature of alteration

Making the assumption that Mnz2 formed in equilibrium with Xnt and Thr, which appears to be the case for the Ambato and Arendal monazites based on the occurrence of the latter phases in Mnz2 domains, it is possible to estimate the temperature of alteration to form this assemblage (Gratz and Heinrich, 1997; Seydoux-Guillaume et al., 2002b) (Table 1). For the Ambato monazite, these calculations yield temperatures ranging from 210 °C (using Th content of monazite; after Seydoux-Guillaume et al., 2002b) to 319 °C (using Y content of monazite; after Gratz and Heinrich, 1997). For Arendal, the crystallization temperature of the Mnz2–Xnt–Thr assemblage (Table 1) is even lower and ranges from 43 °C (using the Th content of monazite; after Seydoux-Guillaume et al., 2002b) to 136 °C (using Y content of monazite; after Gratz and Heinrich, 1997). Nevertheless, it must be emphasized that the very large standard deviation obtained for Y in Mnz2 (Table 1), related to high relative variations in Y at low Y-concentrations (e.g. 0.34 to 0.87 wt.% and 0 to 1.2 wt.% for Ambato and Arendal monazite samples respectively) in monazite samples, leads to large temperature uncertainties, and hence the calculated temperatures should be used with caution. Although disequilibrium between these grains cannot be excluded, the Mnz–Xnt thermometry indicates that alteration took place at low temperatures (<320 °C).

### 5.5. Mass balance calculations

The chemical compositions reported in Tables 1 and 2 were used to perform some elementary mass balance calculations for the proposed reactions, based on the most immobile elements. For Sri Lanka monazite the proposed reaction is:

$$\text{Mnz1} = \text{Mnz2} + \text{thorite} + \text{thorianite}.$$

In this case the amount of Mnz2 produced is initially calculated from Ce + La + Nd, Thr from $SiO_2$, and Thn from $ThO_2$. This calculation, however, does not produce satisfactory results, because after Thr is formed using the available $SiO_2$, no Th is left to form Thn. This suggests that the appearance of Thn is due to a local deficit of $SiO_2$, so that the consumption of $SiO_2$ by Thr leaves an excess of Th that must be incorporated in Thn. With the simpler reaction:

$$\text{Mnz1} = \text{Mnz2} + \text{Thr}$$

and based on balancing for La, Ce and Nd in the Sri Lanka monazite, we calculate that 1 g of Mnz1 can produce 0.76 g of Mnz2. The remaining Th allows 0.27 g of Thr to be made. This reaction produces an excess of Si, P and U but requires some Ca to balance the reaction. Assuming that density of monazite is 5.3 g/cm$^3$ and that of thorite 6.8 g/cm$^3$, we

can estimate that 0.189 $cm^3$ of Mnz1 produces 0.143 $cm^3$ of Mnz2 and 0.039 $cm^3$ of Thr, yielding a 3.6:1 volume ratio. The volumetric proportion of the two phases can also be estimated by analyzing SEM images, using the assumption that the area proportions are approximately equivalent to the volume proportions for the random distribution of Thr in Mnz2. Processing of the image in Fig. 2b yielded a Mnz2/Thr area ratio of 4.1, in reasonable agreement with the simplified mass balance calculations described above.

For the Arendal and Ambato samples, xenotime, estimated from Y, must be added as reaction product; the proposed reaction becomes:

$$\text{Mnz1} = \text{Mnz2} + \text{Thr} + \text{Xnt}.$$

Using the same method and assuming that the density of xenotime is 4.3 $g/cm^3$ we calculate that, for Ambato, 0.88 g of Mnz2, 0.12 g of Thr and 0.10 g of Xnt are produced for each gram of Mnz1 consumed, or 0.166 $cm^3$, 0.018 $cm^3$, 0.023 $cm^3$ for each $cm^3$ of Mnz1 transformed. With these phase proportions, some excess $SiO_2$ and U remain. For Arendal we obtained 0.87 g Mnz2, 0.10 g Thr, and 0.04 g Xnt forming from Mnz1, and 0.92 g Mnz2, 0.03 g Thr, 0.05 g Xnt from Mnz1′. With those phase proportions U is only liberated by the alteration of Mnz1′. Unfortunately, the microtextures of these two samples are too complex for reliable image analysis to be performed in order to compare the predictions of the mass balance modeling with observed modal proportions.

## 6. Geochronology

### 6.1. Chemical Th–U–total Pb ages with EPMA

Results of EMPA dating are reported in Tables 3 to 6. The ages were calculated following the approach of Montel et al. (1996). The data are plotted using the isochron-like diagram of Suzuki and Adachi (1991) in Fig. 8. This representation requires the transformation of the U content into "fictive Th" content, i.e. the amount of Th that would give the same amount of Pb as U for a given age. The sum of the "fictive Th" and the real Th corresponds to the "equivalent Th" value, Th*. The plot of Pb vs Th* should give a straight line, the slope of which yields the age and the intercept at the origin the initial Pb content (assuming that is constant). More details about these methods can be found in Harrison et al. (2002).

For the Sri-Lanka monazite sample, Mnz1 yielded ages from 454 ± 37 to 517 ± 42 Ma and Mnz2 from 472 ± 152 to 576 ± 135 Ma. From a statistical point of view, all ages must be considered to belong to

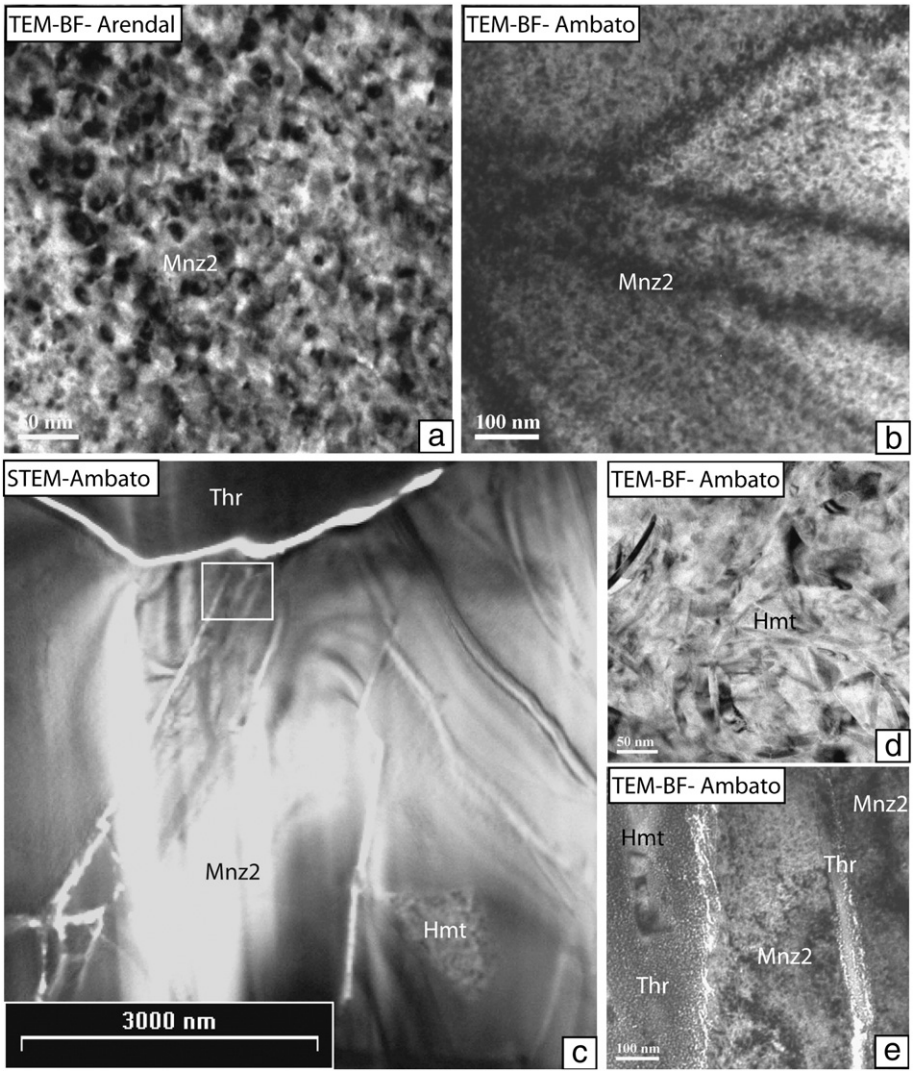


**Fig. 5.** Transmission Electron Microscope (TEM) images of Arendal (a) and Ambato (b–e) monazites. TEM bright field (BF) images of the Arendal (a) and the Ambato (b) monazite samples showing mottled diffraction contrasts reflecting radiation damage. c—Scanning TEM image of the Ambato monazite with many cracks, filled with thorite (Thr), passing through monazite. d—TEM BF image of a hematite (Hmt) pocket (detail from panel c). e—TEM BF image of the Ambato monazite—the enlargement from panel c shows cracks filled with Thr and Hmt inclusions in altered monazite (Mnz2).

**Table 1**
Representative electron microprobe analyses of monazites.

| Sample | Sri Lanka monazite | | | | Ambato monazite | | | | Arendal monazite | | | | | |
|---|---|---|---|---|---|---|---|---|---|---|---|---|---|---|
| | Unaltered | | Altered | | Unaltered | | Altered | | Unaltered 1 | | Unaltered 1′ | | Altered | |
| wt.% | av. 22 anal. | ±2σ | av. 5 anal. | ±2σ | av. 15 anal. | ±2σ | av. 7 anal. | ±2σ | av. 10 anal. | ±2σ | av. 8 anal. | ±2σ | av. 28 anal. | ±2σ |
| $SiO_2$ | 4.7 | 0.4 | 0.6 | 0.1 | 3.1 | 0.5 | 1.2 | 0.3 | 2.1 | 0.2 | 1.1 | 0.1 | 0.7 | 0.3 |
| $P_2O_5$ | 21.8 | 0.6 | 28.4 | 0.6 | 24.3 | 0.7 | 27.4 | 0.6 | 26.6 | 0.3 | 28.2 | 0.3 | 28.7 | 0.5 |
| CaO | 0.6 | 0.1 | 0.7 | 0.2 | 0.2 | 0.1 | 0.2 | 0.1 | 0.9 | 0.1 | 0.9 | 0.0 | 0.8 | 0.2 |
| $Y_2O_3$ | 0.6 | 0.0 | 0.5 | 0.2 | 1.0 | 0.1 | 0.6 | 0.2 | 2.2 | 0.2 | 2.8 | 0.1 | 0.5 | 0.3 |
| $La_2O_3$ | 12.0 | 0.6 | 15.9 | 0.4 | 6.6 | 0.3 | 7.4 | 0.3 | 11.1 | 0.4 | 12.0 | 0.2 | 12.2 | 0.6 |
| $Ce_2O_3$ | 23.4 | 0.1 | 30.8 | 0.6 | 23.9 | 0.9 | 27.3 | 0.8 | 25.5 | 0.5 | 27.0 | 0.3 | 29.0 | 1.3 |
| $Pr_2O_3$ | 2.5 | 0.4 | 3.2 | 0.2 | 3.7 | 0.4 | 4.5 | 0.5 | 3.1 | 0.4 | 3.2 | 0.4 | 3.6 | 0.4 |
| $Nd_2O_3$ | 8.1 | 0.6 | 10.6 | 0.5 | 14.7 | 0.6 | 17.0 | 0.8 | 10.6 | 0.4 | 11.2 | 0.3 | 13.1 | 0.8 |
| $Sm_2O_3$ | 1.0 | 0.3 | 1.4 | 0.4 | 4.4 | 0.3 | 5.0 | 0.4 | 2.1 | 0.4 | 2.2 | 0.4 | 2.6 | 0.4 |
| $Gd_2O_3$ | 0.5 | 0.5 | 0.9 | 0.2 | 1.9 | 0.4 | 2.3 | 0.2 | 1.5 | 0.2 | 1.8 | 0.3 | 1.6 | 0.4 |
| $Dy_2O_3$ | 0.2 | 0.2 | 0.1 | 0.1 | 0.2 | 0.1 | 0.1 | 0.1 | 0.7 | 0.3 | 0.7 | 0.1 | 0.3 | 0.2 |
| PbO | 0.6 | 0.3 | 0.1 | 0.1 | 0.4 | 0.2 | 0.2 | 0.2 | 0.6 | 0.2 | 0.4 | 0.2 | 0.2 | 0.2 |
| $ThO_2$ | 22.9 | 0.1 | 5.5 | 0.6 | 14.1 | 2.1 | 5.8 | 1.6 | 12.0 | 1.2 | 7.3 | 0.5 | 6.2 | 2.0 |
| $UO_2$ | 0.8 | 0.2 | 0.1 | 0.1 | 0.6 | 0.2 | 0.1 | 0.1 | 0.7 | 0.1 | 0.7 | 0.1 | 0.1 | 0.2 |
| Total | 99.7 | | 98.7 | | 99.0 | | 99.0 | | 99.7 | | 99.4 | | 99.6 | |
| Th/U | 29.9 | | 63.9 | | 25.4 | | 70.9 | | 17.9 | | 10.7 | | 48.1 | |
| Cations/4O | | | | | | | | | | | | | | |
| Si | 0.20 | | 0.03 | | 0.13 | | 0.05 | | 0.08 | | 0.04 | | 0.03 | |
| P | 0.79 | | 0.97 | | 0.86 | | 0.95 | | 0.91 | | 0.95 | | 0.97 | |
| Ca | 0.03 | | 0.03 | | 0.01 | | 0.01 | | 0.04 | | 0.04 | | 0.04 | |
| Y | 0.01 | | 0.01 | | 0.02 | | 0.01 | | 0.05 | | 0.06 | | 0.01 | |
| La | 0.19 | | 0.24 | | 0.10 | | 0.11 | | 0.17 | | 0.18 | | 0.18 | |
| Ce | 0.37 | | 0.45 | | 0.37 | | 0.41 | | 0.38 | | 0.39 | | 0.42 | |
| Pr | 0.04 | | 0.05 | | 0.06 | | 0.07 | | 0.05 | | 0.05 | | 0.05 | |
| Nd | 0.12 | | 0.15 | | 0.22 | | 0.25 | | 0.15 | | 0.16 | | 0.19 | |
| Sm | 0.01 | | 0.02 | | 0.06 | | 0.07 | | 0.03 | | 0.03 | | 0.04 | |
| Gd | 0.01 | | 0.01 | | 0.03 | | 0.03 | | 0.02 | | 0.02 | | 0.02 | |
| Dy | 0.00 | | 0.00 | | 0.00 | | 0.00 | | 0.01 | | 0.01 | | 0.00 | |
| Pb | 0.01 | | 0.00 | | 0.00 | | 0.00 | | 0.01 | | 0.00 | | 0.00 | |
| Th | 0.22 | | 0.05 | | 0.13 | | 0.05 | | 0.11 | | 0.07 | | 0.06 | |
| U | 0.01 | | 0.00 | | 0.01 | | 0.00 | | 0.01 | | 0.01 | | 0.00 | |
| Total | 2.01 | | 2.01 | | 2.01 | | 2.01 | | 2.01 | | 2.01 | | 2.01 | |
| U + Th + Pb + Si | 0.44 | | 0.08 | | 0.27 | | 0.10 | | 0.21 | | 0.12 | | 0.09 | |
| ∑REE + Y + P | 1.54 | | 1.90 | | 1.72 | | 1.89 | | 1.76 | | 1.85 | | 1.88 | |
| $X_Y$[a] | | | | | | | 0.03 | 0.01 | | | | | 0.02 | 0.02 |
| T (°C)[a] | | | | | | | 319 | ±120 | | | | | 136 | ±240 |
| T (°C)[b] | | | | | | | 210 | ±140 | | | | | 43 | ±220 |

[a] Calculated after Gratz and Heinrich (1997)—$X_Y$ is the mole fraction Y in monazite assuming a total occupancy of 1 in a Ce–Y system and considering that monazite crystallized in equilibrium with xenotime.
[b] Calculated after Seydoux-Guillaume et al. (2002b)—$X_Y$ is the mole fraction Y in monazite assuming a total occupancy of 1 in a Ce–Y–Th system (and XTh = 0.09) and assuming that monazite crystallized in equilibrium with xenotime and thorium silicate.

one single population, the best estimate of which is 491 ± 9 Ma, with MSWD = 0.74 (n = 24).

For the Ambato monazite sample, Mnz1 yielded ages from 495 ± 75 to 604 ± 104 Ma. Due to the high density of inclusions and fractures, only two measurements can be considered to unambiguously belong to Mnz2; one of these two measurements is chemically similar to Mnz1 (#18 in Table 4), but the other one is significantly lower in Th and U. Mnz1 defines a homogeneous population with a best age estimate at 537 ± 16 Ma. The two measurements in Mnz2 yielded a significantly older age, at 750 ± 33 Ma. The global MSWD is 0.83 (n = 19).

The Arendal monazite sample displays more variable U and Th contents. The Th contents in pristine areas define two groups of analyses: a Th-rich one (about 10 wt.% Th–Mnz1) and a Th-poor one (about 6 wt.% Th–Mnz1′). The Th content in the Mnz2 areas ranges from 2.7 wt.% to 8.4 wt.%, but most values are in the 3–5 wt.% Th range. Resulting ages are of 840 ± 76 to 984 ± 107 Ma for pristine zones (Mnz1 and 1′), and 791 ± 144 to 1247 ± 277 Ma for Mnz2. The whole set of data can be fitted to a single-aged population with a best age estimate at 934 ± 21 Ma (n = 37; MSWD = 1.17).

### 6.2. U/Pb and Th/Pb ages with LA-ICP-MS (Tables 6–8; Figs. 9 and 10)

U–Th–Pb isotopic analysis was carried out on the three monazite crystals. Analytical points were chosen both in the unaltered and altered zones of monazite grains; the locations of analyses are shown in Figs. 2–4. Results are listed in Tables 6–8 and presented graphically in $^{206}Pb/^{238}U$ vs $^{208}Pb/^{232}Th$ modified concordia and in Tera Wasserburg (TW—$^{207}Pb/^{206}Pb$ vs $^{238}U/^{206}Pb$) diagrams in Fig. 9.

Twenty-four analyses were obtained on the Sri Lanka monazite (Table 6, Fig. 2), 18 in Mnz1 and 6 in Mnz2. The results from Mnz1 (18 measurements) yield a weighted $^{206}Pb/^{238}U$ mean (WM) age of 500 ± 5 Ma [MSWD = 3.1] and a WM $^{208}Pb/^{232}Th$ age of 491 ± 4 Ma [MSWD = 2.4] (Fig. 9a and b). The latter age is indistinguishable from the EPMA age (491 ± 9 Ma). $^{207}Pb/^{206}Pb$ and $^{206}Pb/^{238}U$ ages for Mnz2 are widely scattered (from 698 ± 127 to 4105 ± 88 Ma and from 483 ± 23 to 1737 ± 67 Ma, respectively), and are interpreted to reflect the incorporation of common Pb. A regression through data from Mnz2 analyses defines an intercept age of 484 ± 39 Ma (Fig. 9a). Corresponding $^{208}Pb/^{232}Th$ ages are less scattered (from 435 ± 10 to 483 ± 11 Ma), showing younger ages compared to Mnz1 with WM $^{208}Pb/^{232}Th$ apparent ages of 450 ± 18 Ma [MSWD = 11.7].

Twenty one analyses were obtained from the Ambato monazite (Table 7, Fig. 3): thirteen in Mnz1 and eight in Mnz2. In the case of Mnz1 two analyses (#48 and 49) display higher $^{207}Pb/^{206}Pb$ ratios and demonstrate common Pb contamination, probably due to their proximity to both cracks and (Th,U)-silicate inclusions (Fig. 3); these analyses were not considered in the calculation of WM ages for Mnz1. The remaining analyses yield a WM $^{206}Pb/^{238}U$ age of 514 ± 6 Ma

**Table 2**
Representative electron microprobe analyses of Th-rich phases (thorianite and $ThSiO_4$) and xenotime.

| Sample | Sri Lanka monazite | | | | Ambato monazite | | | | Arendal monazite | | | |
|---|---|---|---|---|---|---|---|---|---|---|---|---|
| Characteristics | Thorianite | | $ThSiO_4$ | | $ThSiO_4$ | | Xenotime | | $ThSiO_4$ | | Xenotime | |
| wt.% | av. 6 anal. | ±2σ | av. 5 anal. | ±2σ | av. 2 anal. | ±2σ | av. 8 anal. | ±2σ | av. 6 anal. | ±2σ | av. 10 anal. | ±2σ |
| $SiO_2$ | 0.34 | 0.20 | 12.99 | 1.42 | 8.91 | 0.73 | 0.01 | 0.02 | 16.39 | 0.65 | 0.00 | |
| $P_2O_5$ | – | | – | | – | | 35.20 | 0.41 | 0.56 | 0.24 | 34.51 | 0.43 |
| $V_2O_5$ | 0.05 | 0.05 | 0.25 | 0.14 | 0.17 | 0.07 | – | | – | | – | |
| $As_2O_5$ | 0.01 | 0.02 | 0.00 | | 0.06 | 0.06 | – | | – | | – | |
| $SO_2$ | 0.30 | 0.09 | 0.12 | 0.09 | 0.03 | 0.02 | – | | – | | – | |
| CaO | 0.72 | 0.26 | 1.10 | 0.12 | 0.17 | 0.14 | 0.01 | 0.01 | 2.01 | 0.38 | 0.01 | 0.01 |
| FeO | 0.55 | 0.55 | 1.30 | 2.95 | 0.09 | 0.10 | 0.00 | | – | | 0.00 | |
| MnO | 0.02 | 0.04 | 0.03 | 0.05 | – | – | 0.02 | 0.02 | – | | 0.01 | 0.02 |
| $Y_2O_3$ | 0.03 | 0.01 | 0.89 | 0.36 | – | | 48.33 | 0.59 | 0.51 | 0.37 | 44.32 | 0.61 |
| $La_2O_3$ | – | | – | | – | | 0.07 | 0.06 | 0.00 | 0.01 | 0.05 | 0.05 |
| $Ce_2O_3$ | – | | – | | – | | 0.12 | 0.06 | 0.00 | 0.01 | 0.05 | 0.06 |
| $Pr_2O_3$ | – | | – | | – | | – | | 0.09 | 0.19 | – | |
| $Nd_2O_3$ | – | | – | | – | | 0.15 | 0.10 | 0.10 | 0.16 | 0.22 | 0.15 |
| $Sm_2O_3$ | – | | – | | – | | 1.16 | 0.14 | 0.04 | 0.04 | 0.46 | 0.21 |
| $Gd_2O_3$ | – | | – | | – | | 5.74 | 0.55 | 0.09 | 0.14 | 4.95 | 0.42 |
| $Tb_2O_3$ | – | | – | | | | 1.00 | 0.16 | | | 1.03 | 0.16 |
| $Dy_2O_3$ | 0.07 | 0.10 | 0.13 | 0.19 | – | | 5.35 | 0.18 | 0.30 | 0.35 | 7.98 | 0.60 |
| $Ho_2O_3$ | – | | – | | | | 0.24 | 0.27 | – | | 1.12 | 0.39 |
| $Er_2O_3$ | 0.06 | 0.10 | 0.15 | 0.08 | – | | 0.81 | 0.17 | – | | 3.27 | 0.25 |
| $Tm_2O_3$ | – | | – | | – | | 0.00 | | – | | 0.16 | 0.12 |
| $Yb_2O_3$ | – | | – | | – | | 0.08 | 0.10 | – | | 1.28 | 0.27 |
| $Lu_2O_3$ | – | | – | | – | | 0.20 | 0.32 | – | | 0.15 | 0.25 |
| PbO | 0.05 | 0.08 | 0.17 | 0.16 | 0.15 | 0.08 | 0.03 | 0.05 | 0.11 | 0.10 | 0.05 | 0.07 |
| $ThO_2$ | 88.53 | 3.00 | 72.65 | 4.61 | 72.22 | 1.22 | 0.51 | 0.56 | 62.90 | 0.61 | 0.34 | 0.34 |
| $UO_2$ | 0.71 | 0.18 | 1.91 | 0.50 | 2.57 | 0.58 | 0.13 | 0.13 | 6.99 | 0.48 | 0.11 | 0.11 |
| Total | 91.45 | | 91.69 | | 84.37 | | 99.12 | | 90.08 | | 100.06 | |
| Th/U | 125 | | 38 | | 28 | | 4 | | 9 | | 3 | |
| Cations/4O | | | | | | | | | | | | |
| U + Th + Pb + Si | | | 1.90 | | 1.97 | | 0.01 | | 1.88 | | 0.00 | |
| ∑ REE + Y + P | | | 0.02 | | 0.03 | | 2.00 | | 0.06 | | 2.01 | |
| Total | | | 1.92 | | 2.00 | | 2.01 | | 1.94 | | 2.01 | |

[MSWD = 9; n = 11]. In the modified Concordia diagram, data are concordant and yield a WM $^{208}Pb/^{232}Th$ age (Fig. 9d) of 507 ± 7 Ma [MSWD = 13; n = 11], younger than but close to the EPMA age (537 ± 16 Ma for Mnz1—see above). Mnz2 data show considerable scatter, along with data high degree of discordance (Fig. 9c and d: 3261 to 4908 Ma for $^{207}Pb/^{206}Pb$ ages, 611 to 5565 Ma for $^{206}Pb/^{238}U$ ages, and 294 to 1022 Ma for $^{208}Pb/^{232}Th$ ages). In this sample most of the Mnz2 analytical points plotting along a discordia line (Fig. 9c) at a position corresponding to ~80% contribution from common Pb ($^{207}Pb/^{206}Pb \sim 0.7$), and it is therefore not possible to define an intercept age for Mnz2. Except for one analysis (#59—see below), all $^{208}Pb/^{232}Th$ apparent ages measured in Mnz2 are significantly older than the $^{208}Pb/^{232}Th$ ages determined for Mnz1 (Table 7, Figs. 9d and 10b). This is consistent with the "old" chemical U–Th–Pb apparent ages obtained by EPMA in the altered areas (750 ± 33 Ma). One analysis (#59) differs strongly from the other Mnz2 data in having very high Th and U contents (22.3 wt.% Th and 8375 ppm U) and lower $^{206}Pb/^{238}U$ and $^{208}Pb/^{232}Th$ ages of 611 ± 7 and 294 ± 3 Ma respectively. These unique features are considered to reflect the incorporation of high (Th,U)-silicate inclusions (see Table 2) in this analysis, an interpretation supported by the similarity between the measured Th/U ratio (= 27) of Mnz2 and that of Th-silicate (= 28—Table 2).

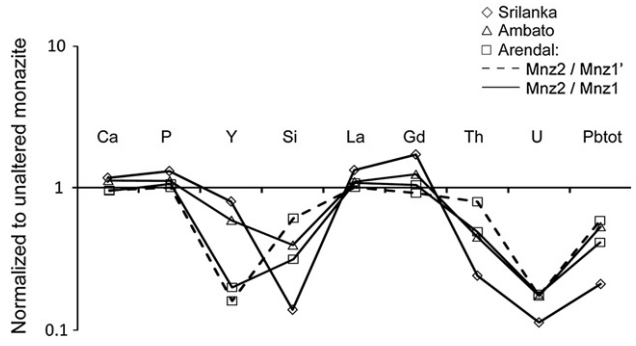


**Fig. 6.** Electron Probe Micro Analyser (EPMA) analyses showing the chemical effects of alteration in the Sri Lanka, Arendal and Ambato monazite samples. The mean value of altered monazite (Mnz2) is normalized to the mean of unaltered analyses (Mnz1). All three monazites have the same pattern reflecting loss of Th, Si, Y, U, and Pb with a preferential loss of U relative to Th leading to an increase of the Th/U ratio.

Twenty-two analyses were obtained from the Arendal monazite (Table 8, Fig. 4), sixteen in the pristine zones (8 for Mnz1 + 8 for Mnz1′) and 6 in Mnz2. The Mnz1 and Mnz1′ data fall slightly below the concordia curve (Fig. 9e). The WM $^{206}Pb/^{238}U$ age for Mnz1 is 917 ± 14 Ma [MSWD = 10.1; n = 8] and for Mnz1′ is 896 ± 9 Ma [MSWD = 4.7; n = 8]. The results for these two magmatic zones statistically overlap and so warrant the pooling of all the data for the pristine monazite. This produces a poorly fitting WM $^{206}Pb/^{238}U$ age of 906 ± 9 Ma [MSWD = 11.6; n = 16]. The corresponding WM $^{208}Pb/^{232}Th$ ages (Fig. 9f) are 909 ± 18 Ma [MSWD = 19; n = 8] for Mnz1 and 892 ± 12 Ma [MSWD = 8.9; n = 8] for Mnz1′, and the pooled WM $^{208}Pb/^{232}Th$ age for both is 900 ± 11 Ma [MSWD = 16; n = 16]. For comparison, the chemical U–Th–Pb age obtained by EPMA (see above) is arguably older (934 ± 21 Ma), but as indicated by the MSWD for Mnz1 and Mnz1′ there is considerable scatter in the isotopic data that preclude a simple interpretation of them as representing a single, geologically-meaningful age. Since Mnz2 $^{206}Pb/^{238}U$ and $^{207}Pb/^{235}U$ ratios are higher than those of Mnz1 these result in Pb–U data with poor precisions (large ellipses in Fig. 9) scattered along the concordia curve, as well as apparent ages equivalent to or older than those of Mnz1 ($^{206}Pb/^{238}U$ ages between 902 ± 15 and 1203 ± 21 Ma). In contrast, $^{208}Pb/^{232}Th$ ages for Mnz2 are on average younger than in

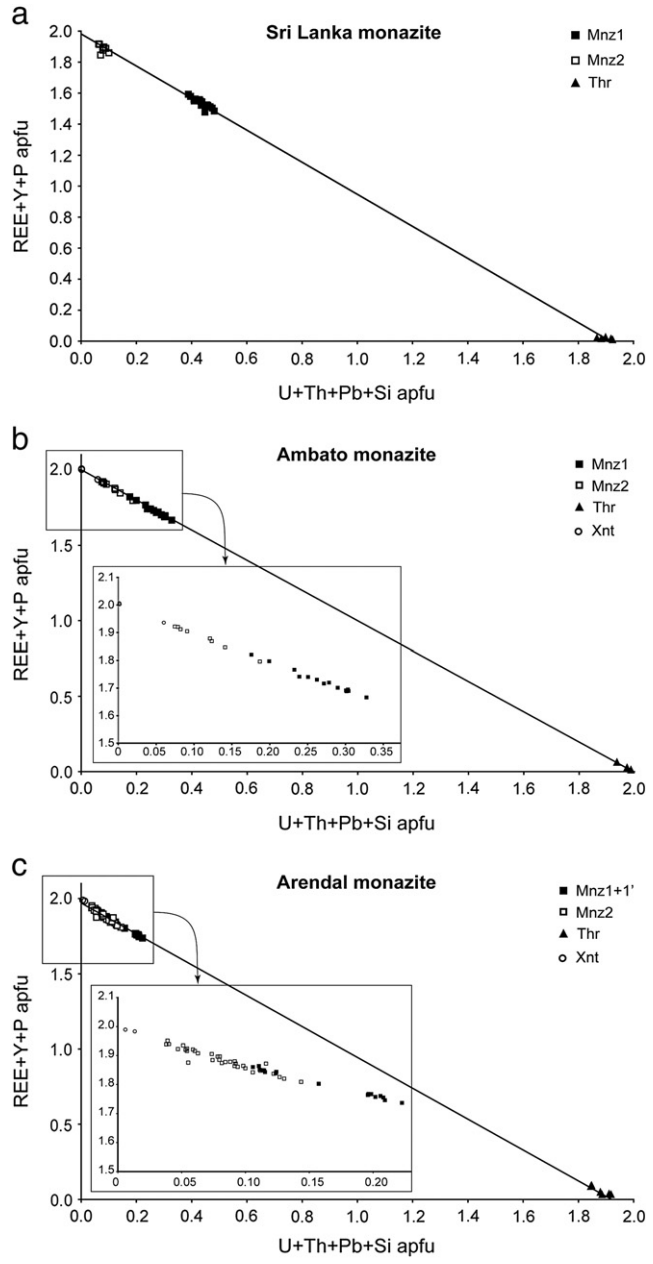


**Fig. 7.** Compositional variation diagrams (REE + Y + P) vs (Th + U + Si + Pb) in atoms per formula unit, for 4 oxygens (apfu) for unaltered (Mnz1 and Mnz1′), altered monazite (Mnz2) and other recrystallized phases, such as Th-rich thorite (Thr) and Y-rich xenotime (Xnt), for the Sri Lanka (a), Ambato (b) and Arendal (c) monazite samples. In all samples, unaltered and altered monazites (Mnz1–1′ and Mnz2) plot along a straight line in the compositional diagram, with xenotime and thorite on both ends of the line.

Mnz1, and are less scattered (from 837 ± 9 to 929 ± 10 Ma) than the $^{206}Pb/^{238}U$ ages (Fig. 9f). Exclusion of analysis #31 (929 ± 10 Ma), which shows considerably higher Th (8.7 wt.%) and U (3266 ppm) concentrations than those typical of Mnz2 (EPMA: 5.8 wt.% Th and 800 ppm U), possibly produced by mixing of Mnz2 and Mnz1′ volumes in the analysis, yields a poorly fitted WM $^{208}Pb/^{232}Th$ age of 864 ± 21 Ma [MSWD = 12; n = 5] for Mnz2.

## 7. Discussion

Large crystals of monazite are unusual mineralogical samples which are difficult to find and collect. The crystals studied here were sourced from mineralogical collections for which location data and geologic context are absent. Therefore, discussion of the nature of the alteration processes is limited, especially concerning the fluids which caused monazite alteration. Despite this we consider that useful data on how monazite reacts with geological fluids at the micro- and nano-scale can still be obtained from these samples.

### 7.1. Alteration conditions and consequences for element mobility

The data presented here confirm the results of a recent study on alteration of xenotime and monazite from granitic pegmatites hosted in an anorthosite, SW Norway (Hetherington and Harlov, 2008). Th and U are incorporated in the three monazite grains studied here (Sri Lanka, Ambato and Arendal) via a substitution mechanism involving both crystallographic sites [$(Th, U)^{4+} + Si^{4+} = (REE, Y)^{3+} + P^{5+}$] of the monazite lattice(9-fold coordinated REE-site and tetrahedral P-site; Ni et al., 1995). The other well-known substitution that occurs in monazite (Friedrich et al., 1987; Franz et al., 1996; Förster, 1998) involving Ca on one crystallographic site [$(Th, U)^{4+} + Ca^{2+} = 2\,(REE, Y)^{3+}$] is negligible in these samples, consistent with a low concentration or availability of Ca in the environment of monazite growth in these samples. For all monazite samples, the composition of the unaltered monazites (Mnz1) plots along a straight line between the two product phases, a Th-rich phase (thorite) on one side and one corresponding to secondary monazite (Mnz2) on the other (Fig. 7). In the case of the Ambato and Arendal monazites, in which the Y content is higher in the unaltered monazite, newly-formed xenotime plots at one end of the compositional line (Fig. 7b and c). An interesting point concerns the increase of Th/U ratio in monazites during hydrothermal alteration (Table 1); from 30 to 64 in the case of Sri Lanka monazite, 25 to 71 for the Ambato and 18 to 48 for the Arendal monazite samples. Such a difference has previously been observed in some hydrothermally altered monazites by Poitrasson et al. (2000) in the Skiddaw granite, in hydrothermal monazite by Janots et al. (2012) and in monazite from granitic pegmatites from Norway by Hetherington and Harlov (2008). This trend is the consequence of a chemical fractionation between U and Th during alteration (greater loss of U than of Th). Furthermore, while some U is incorporated in the Th-rich phase (Table 2) no U-rich phase such as coffinite or uraninite formed. The mass balance calculations show that some uranium is liberated from the system during the reaction, which could have important consequences, as far as the formation of uranium deposits is concerned.

The temperature estimates obtained here for Ambato and Arendal monazite grains (<320 °C), are consistent with previous examples in which monazite is altered by moderate-temperature fluids (Poitrasson et al., 2000; Mathieu et al., 2001). However, none of the experimental studies so far have been able to reproduce the specific alteration textures as described in the three samples of this study, i.e. secondary monazite associated with thorite and xenotime. To our knowledge, the only experimental evidence for a Th-rich phase forming as the result of monazite alteration via dissolution in the presence of fluid is thorianite that crystallized during the experiments of Seydoux-Guillaume et al. (2002a) in the presence of pure $H_2O$ fluid over the temperature range of 800–1200 °C. It is also known from the experiments that at high temperatures above 600 °C large amounts of $ThSiO_4$ can be entirely substituted into the monazite lattice (Seydoux-Guillaume et al., 2002b; Hetherington et al., 2010; Harlov et al., 2011). Under such conditions (i.e. alkaline fluids–high temperatures; see Introduction), Th-rich monazite forms at the reaction front between unaltered and altered monazites (Figs. 2–4 in Seydoux-Guillaume et al., 2002b; Figs. 6–7 in Harlov et al., 2011). These results demonstrate the need for experimental studies and modeling of monazite alteration at low temperature (<320 °C).

Considering now the alteration mechanism, two possible processes can be distinguished: solid state exsolution (= volume diffusion) and coupled dissolution–precipitation in the presence of fluid. Although as noted above monazite is able to incorporate high amounts

**Table 3**
Analytical data for the Sri Lanka monazite (EPMA).

| # | U (ppm) | ± (2σ) | Th (ppm) | ± (2σ) | Pb (ppm) | ± (2σ) | Th* | Age (Ma) | ± (2σ) |
|---|---|---|---|---|---|---|---|---|---|
| 1 | 6531 | 274 | 212,496 | 1840 | 4772 | 338 | 233,935 | 454 | 37 |
| 2 | 6346 | 273 | 192,181 | 1737 | 4728 | 341 | 213,078 | 494 | 41 |
| 3 | 6420 | 272 | 190,708 | 1725 | 4545 | 340 | 211,820 | 477 | 41 |
| 4 | 6841 | 275 | 203,082 | 1791 | 5003 | 343 | 225,607 | 493 | 39 |
| 5 | 7040 | 276 | 207,873 | 1816 | 5365 | 341 | 231,095 | 516 | 38 |
| 6 | 7102 | 275 | 206,837 | 1808 | 5331 | 343 | 230,260 | 514 | 39 |
| 7 | 612 | 232 | 49,317 | 915 | 1091 | 318 | 51,329 | 472 | 152 |
| 8 | 561 | 230 | 44,885 | 884 | 1168 | 314 | 46,741 | 555 | 167 |
| 9 | 688 | 229 | 41,275 | 856 | 1000 | 317 | 43,543 | 510 | 179 |
| 10 | 495 | 231 | 43,104 | 875 | 1048 | 317 | 44,737 | 520 | 175 |
| 11 | 1026 | 233 | 53,263 | 943 | 1246 | 315 | 56,640 | 489 | 137 |
| 12 | 915 | 234 | 55,601 | 953 | 1523 | 316 | 58,634 | 576 | 135 |
| 13 | 630 | 231 | 46,492 | 900 | 1218 | 314 | 48,577 | 557 | 161 |
| 14 | 6441 | 272 | 189,583 | 1721 | 4709 | 339 | 210,798 | 497 | 41 |
| 15 | 6644 | 273 | 192,683 | 1740 | 4580 | 341 | 214,527 | 474 | 41 |
| 16 | 6800 | 273 | 197,739 | 1761 | 4915 | 340 | 220,136 | 497 | 40 |
| 17 | 6961 | 275 | 208,764 | 1820 | 4980 | 343 | 231,657 | 478 | 38 |
| 18 | 7359 | 276 | 212,668 | 1838 | 5339 | 343 | 236,912 | 500 | 37 |
| 19 | 7298 | 277 | 215,401 | 1852 | 5188 | 345 | 239,410 | 482 | 37 |
| 20 | 7038 | 276 | 208,371 | 1820 | 4834 | 345 | 231,494 | 465 | 38 |
| 21 | 6691 | 273 | 196,501 | 1758 | 4939 | 341 | 218,548 | 502 | 40 |
| 22 | 6747 | 274 | 195,130 | 1750 | 4856 | 342 | 217,353 | 497 | 41 |
| 23 | 6204 | 270 | 185,983 | 1701 | 4800 | 338 | 206,449 | 517 | 42 |
| 24 | 6549 | 273 | 194,869 | 1749 | 4774 | 339 | 216,429 | 491 | 40 |

Th* corresponds to Th+the equivalent of U (after Suzuki and Adachi, 1991).
Cells in gray correspond to Mnz2.

of $ThSiO_4$ and $YPO_4$ at high temperatures, at lower temperature a miscibility gap exists (Gratz and Heinrich, 1997; Heinrich et al., 1997; Seydoux-Guillaume et al., 2002b). As a result, Th and Y should be excluded from monazite lattice at low temperatures ($\ll$600 °C). Solid state exsolution of thorite and xenotime at low temperature is highly unlikely because of the very slow diffusion kinetics in monazite (Cherniak and Pyle, 2008). The sharp interfaces between different phases, the presence of cracks and porosity (Figs. 2–5), and the sharp boundaries between thorite and monazite on the TEM images (Fig. 5c) instead are supportive of a dissolution–precipitation mechanism facilitated by a fluid medium (see review in Putnis, 2009). The key observation about the alteration mechanism of these monazite samples is that it does not correspond to pseudomorphic replacement (i.e. dissolution–precipitation coupled at the interface of the parent and product phases with preservation of the external morphology of the parents), as is commonly observed in nature and experiments (see review in Putnis, 2009). In the present study dissolution, and associated precipitation, began and progressed via a pre-existing fracture network, allowing access and pathways for fluid. In contact with a reactive low temperature fluid (<320 °C), the Th-(±Y)-rich magmatic monazite (Mnz1) became unstable and dissolved. The interfacial fluid became supersaturated, leading to the precipitation of new mineral phases, i.e. Th–Y-depleted monazite (Mnz2), thorite, ± xenotime, less soluble in the fluid than the original Mnz1 (see also Bilal et al., 1998; Seydoux-Guillaume et al., 2007; Hetherington and Harlov, 2008; Putnis, 2009). Although the composition of the fluid in this study is unknown, it must have been Fe-bearing, because hematite precipitated within Mnz2 and along cracks (Figs. 1 and 5). It is important to emphasize the essential role of porosity and cracks, which allow fluid migration through the samples during this process. In the next section the role and origin of fracturing (hydration, radiation damage induced swelling, volume change due to phase transformation) will be discussed.

### 7.2. Effects of radiation damage

Over geological time, U- and Th-rich minerals, like monazite and thorite, accumulate radiation damage, mainly from α-decay. Radiation destroys the host crystal lattice to a variable extent, in some cases leading to an amorphous structure, called the metamict state (see summary in Ewing, 1994). Collision cascades due to the alpha-recoil nuclei (=daughter nuclei) are the main cause of amorphization of the crystal lattice. Although daughter nuclei are less energetic (100–400 keV) and less penetrative (20–50 nm) than α-particles emitted during α-decay,

**Table 4**
Analytical data for the Ambato monazite (EPMA).

| # | U (ppm) | ± (2σ) | Th (ppm) | ± (2σ) | Pb (ppm) | ± (2σ) | Th* | Age (Ma) | ± (2σ) |
|---|---|---|---|---|---|---|---|---|---|
| 1 | 3379 | 253 | 106,460 | 1283 | 2599 | 354 | 117,584 | 491 | 75 |
| 2 | 5802 | 264 | 127,523 | 1402 | 3247 | 361 | 146,626 | 492 | 62 |
| 3 | 6015 | 265 | 134,659 | 1442 | 3491 | 361 | 154,478 | 502 | 59 |
| 4 | 5751 | 262 | 118,379 | 1356 | 3227 | 357 | 137,358 | 522 | 65 |
| 5 | 5881 | 264 | 131,370 | 1427 | 3582 | 362 | 150,787 | 528 | 60 |
| 6 | 6080 | 265 | 135,108 | 1448 | 3705 | 358 | 155,186 | 530 | 58 |
| 7 | 5913 | 265 | 134,262 | 1446 | 3683 | 362 | 153,791 | 532 | 59 |
| 8 | 5913 | 266 | 132,201 | 1432 | 3665 | 358 | 151,738 | 537 | 60 |
| 9 | 5145 | 260 | 122,998 | 1380 | 3399 | 356 | 140,000 | 539 | 64 |
| 10 | 4120 | 254 | 87,831 | 1176 | 2482 | 353 | 101,450 | 543 | 87 |
| 11 | 3465 | 247 | 69,118 | 1062 | 1982 | 349 | 80,575 | 546 | 107 |
| 12 | 5519 | 264 | 148,250 | 1516 | 4105 | 363 | 166,501 | 548 | 55 |
| 13 | 4283 | 253 | 89,639 | 1190 | 2594 | 352 | 103,810 | 555 | 85 |
| 14 | 4045 | 254 | 102,449 | 1260 | 2948 | 352 | 115,844 | 565 | 77 |
| 15 | 5428 | 259 | 109,981 | 1311 | 3262 | 355 | 127,957 | 566 | 70 |
| 16 | 6036 | 263 | 119,891 | 1367 | 3786 | 356 | 139,934 | 600 | 65 |
| 17 | 3516 | 248 | 73,524 | 1089 | 2321 | 353 | 85,203 | 604 | 104 |
| 18 | 2327 | 244 | 110,085 | 1301 | 3986 | 357 | 117,905 | 747 | 79 |
| 19 | 1326 | 237 | 68,560 | 1055 | 2503 | 347 | 73,020 | 758 | 122 |

Th* corresponds to Th+the equivalent of U (after Suzuki and Adachi, 1991).
Cells in gray correspond to Mnz2.

they are heavier, and thus more destructive (800–2000 displacement/particle) than α-particles (e.g. Ewing et al., 1995; Nasdala et al., 1996; Weber et al., 1998; Ewing et al., 2000). The balance between damage accumulation and annealing controls the metamictization, i.e. the amorphization of the host mineral. Annealing may be due to temperature, or to other more complex processes, such as healing by alpha particles (Ouchani et al., 1997). Monazite is well known to remain in a crystalline state, because its lattice repairs faster than it is destroyed, even at low temperatures (60–200 °C depending on its composition—Meldrum et al., 1997). In natural monazite, clear evidence of radiation damage has been shown to be limited to isolated nm-sized domains within the crystal (Black et al., 1984; Meldrum et al., 1998; Seydoux-Guillaume et al., 2002c, 2003, 2004, 2007; Nasdala et al., 2010). This study confirms these results as the TEM observations demonstrate the same brightness contrasts in both Arendal and Ambato monazites (Fig. 5a–b), characteristics that result from the presence of very little lattice distortion and corresponding to moderate degrees of accumulated radiation damage, as observed in previous studies (Black et al., 1984; Meldrum et al., 1998; Seydoux-Guillaume et al., 2002c, 2003, 2004, 2007; Nasdala et al., 2010). In contrast, thorite has been found mostly in a metamict (i.e. amorphous) state (Pabst, 1952; Lumpkin and Chakoumakos, 1988; Farges and Calas, 1991). Observations using TEM on the inclusions in the Arendal monazite (Seydoux-Guillaume et al., 2007) and the Ambato monazite (Fig. 5c) also point to an amorphous state for the secondary (i.e. within altered monazite) thorite.

The most important consequence for rocks containing radioactive minerals is that the long-time scale integration of these atomic-scale interactions (amorphization) will dramatically change the physical properties of the radioactive host minerals (e.g. Weber et al., 1998). The present study shows that swelling can trigger intense fracturing within and around secondary radioactive minerals (see also Lee and Tromp, 1995; Nasdala et al., 2010; Seydoux-Guillaume et al., 2007, 2009). These fractures can be interconnected to form a network, and so constitute an efficient way for fluids to pass through the monazite host crystals.

In the Sri Lanka sample, the large cracks that traverse through the entire crystal (Fig. 1a) originate at the Th-rich inclusions and secondary monazite (Mnz2) (Fig. 2c) interface, and propagate through the Mnz2 domains (Fig. 2b). These cracks are therefore interpreted to form as a consequence of the swelling of the Th-rich inclusions. Even though these features are more complicated for the two other monazite samples, because their fracture networks are very dense, it again appears that the cracks originate from the thorite inclusions. On smaller scales (Fig. 5) the cracks initiate at the thorite–Mnz2 interface in the Ambato crystal. An interesting observation from some images (Figs. 3, 4 and 5) is that some cracks are partially to completely filled with a Th-rich phase and a Fe-rich phase (hematite; Figs. 1 and 5), providing evidence that late fluid circulation can transport $Fe^{3+}$ and Th over several microns to millimeter scales. This suggests that fluid was continually passing through the monazite for some time after the recrystallization event. This could lead to complications with inferring the "timing" of a specific geological event, because ages could be disturbed for some period after the main event as a consequence of continued fluid ingress and reaction.

Macroscopic swelling due to metamictization can reach 16 vol.%, for Pu-doped zircon (Weber et al., 1994), or 8 vol.%, for externally irradiated $LaPO_4$ monazites (Picot et al., 2008). No data exist for thorite, but it is expected to be similar to zircon, with which it is isostructural. Thorianite, like uraninite, remains crystalline even for high irradiation

**Table 5**
Analytical data for the Arendal monazite (EPMA).

| # | U (ppm) | ± (2σ) | Th (ppm) | ± (2σ) | Pb (ppm) | ± (2σ) | Th* | Age (Ma) | ± (2σ) |
|---|---|---|---|---|---|---|---|---|---|
| 1 | 6226 | 259 | 101,259 | 1254 | 5411 | 362 | 122,582 | 970 | 79 |
| 2 | 5959 | 261 | 102,749 | 1259 | 5491 | 363 | 123,175 | 980 | 79 |
| 3 | 6569 | 263 | 110,904 | 1307 | 5701 | 367 | 133,345 | 941 | 74 |
| 4 | 5823 | 259 | 103,745 | 1265 | 5210 | 365 | 123,613 | 927 | 79 |
| 5 | 6306 | 261 | 104,626 | 1271 | 4792 | 363 | 125,981 | 839 | 76 |
| 6 | 6486 | 256 | 64,085 | 1025 | 3779 | 352 | 86,287 | 964 | 106 |
| 7 | 6245 | 255 | 57,771 | 978 | 3470 | 350 | 79,150 | 965 | 115 |
| 8 | 6060 | 253 | 57,912 | 985 | 3474 | 349 | 78,668 | 971 | 115 |
| 9 | 5974 | 255 | 66,040 | 1036 | 3876 | 353 | 86,525 | 984 | 107 |
| 10 | 6631 | 257 | 62,728 | 1014 | 3701 | 354 | 85,404 | 953 | 108 |
| 11 | 364 | 230 | 32,592 | 802 | 1333 | 337 | 33,828 | 869 | 255 |
| 12 | 740 | 231 | 40,228 | 861 | 1828 | 344 | 42,756 | 940 | 208 |
| 13 | 344 | 230 | 29,304 | 772 | 1102 | 341 | 30,465 | 799 | 283 |
| 14 | 389 | 228 | 27,583 | 761 | 1135 | 345 | 28,903 | 865 | 302 |
| 15 | 1400 | 234 | 56,451 | 973 | 2191 | 344 | 61,173 | 791 | 144 |
| 16 | 527 | 231 | 44,065 | 876 | 1981 | 346 | 45,867 | 950 | 196 |
| 17 | 577 | 231 | 32,925 | 803 | 1584 | 342 | 34,906 | 997 | 254 |
| 18 | 434 | 228 | 29,910 | 780 | 1685 | 344 | 31,424 | 1174 | 289 |
| 19 | 519 | 227 | 30,970 | 775 | 1871 | 341 | 32,793 | 1247 | 277 |
| 20 | 1081 | 233 | 37,966 | 841 | 1974 | 345 | 41,691 | 1039 | 216 |
| 21 | 485 | 231 | 39,387 | 850 | 1949 | 346 | 41,059 | 1042 | 221 |
| 22 | 665 | 231 | 45,338 | 888 | 2044 | 346 | 47,611 | 945 | 189 |
| 23 | 968 | 233 | 57,884 | 980 | 2569 | 346 | 61,186 | 925 | 148 |
| 24 | 742 | 234 | 59,382 | 987 | 2489 | 347 | 61,905 | 885 | 146 |
| 25 | 951 | 232 | 38,386 | 838 | 2010 | 346 | 41,669 | 1059 | 217 |
| 26 | 1375 | 238 | 77,821 | 1111 | 3253 | 351 | 82,489 | 869 | 111 |
| 27 | 520 | 231 | 41,422 | 865 | 2385 | 345 | 43,241 | 1206 | 214 |
| 28 | 1010 | 237 | 72,690 | 1079 | 3017 | 355 | 76,121 | 874 | 122 |
| 29 | 1152 | 233 | 67,026 | 1037 | 3023 | 347 | 70,960 | 938 | 129 |
| 30 | 644 | 231 | 45,009 | 891 | 1827 | 346 | 47,193 | 854 | 188 |
| 31 | 1481 | 238 | 76,710 | 1102 | 3448 | 352 | 81,764 | 928 | 114 |
| 32 | 961 | 235 | 62,401 | 1009 | 2573 | 349 | 65,662 | 864 | 138 |
| 33 | 1108 | 235 | 67,624 | 1042 | 2736 | 348 | 71,378 | 846 | 127 |
| 34 | 2054 | 240 | 84,310 | 1145 | 3900 | 352 | 91,326 | 939 | 102 |
| 35 | 838 | 233 | 49,064 | 920 | 2350 | 346 | 51,940 | 994 | 175 |
| 36 | 564 | 233 | 50,913 | 938 | 2221 | 348 | 52,837 | 926 | 171 |
| 37 | 586 | 231 | 43,914 | 882 | 1830 | 348 | 45,905 | 879 | 195 |

Th* corresponds to Th+the equivalent of U (after Suzuki and Adachi, 1991).
Cells in gray correspond to Mnz2.
Mnz1: #1 to 5 and Mnz1′: #6 to 10.

doses (Evron et al., 1994; Seydoux-Guillaume et al., 2009). Therefore, swelling is not caused by amorphization of thorianite. Another possible process is hydration, as shown by Seydoux-Guillaume et al. (2007). EPMA totals (Table 2) for all the Th-rich phases are low (~90 wt.%), a feature which can be attributed to presence of water. Nasdala et al. (2009) demonstrated that deficient EPMA totals in zircon can be also assigned to the presence of nano-pores; this nanoporous texture is explained by the replacement via a fluid driven reaction of radiation-damaged zircon by a crystalline nanoporous (with smaller volume) zircon (see also Hay and Dempster, 2009). Furthermore, the presence of nanopores allows incorporation of water (or other non-formula elements). The final possible cause of swelling is volume change due to reaction. From the proportions obtained by mass balance (c.f. above), assuming densities of 5.3 g/cm$^3$, 6.7 g/cm$^3$ and 4.3 g/cm$^3$for monazite, thorite and xenotime respectively, we calculated a volume change of about −3% (decrease in volume) in the Sri Lanka, +10% in the Ambato, and 0 (Mnz1) to +1% (Mnz1′) in the Arendal monazite samples. The volume change due to mineral reaction may create porosity or swelling, depending on the precise reaction.

Based on the measured U and Th contents (Table 1) and the corresponding $^{208}$Pb–$^{232}$Th ages (Fig. 9—mean weight averages calculated only on unaltered monazites: 491, 507 and 909 (Mnz1) and 892 (Mnz1′) Ma for Sri Lanka, Ambato and Arendal respectively) it is possible to estimate the theoretical self-irradiation doses (Ewing et al., 2000; Nasdala et al., 2001) received by the monazite grains in this study. These doses, for unaltered monazites, are: $10.1\times10^{19}$ α-decay/g (i.e. 8.5 dpa, displacements per atom), $6.6\times10^{19}$ α-decay/g (5.5 dpa) and $10.7\times1019$ α-decay/g (9 dpa) and $7.35\times10^{19}$ α-decay/g (6.2 dpa) for Sri Lanka, Ambato and Arendal (1–1′) monazites respectively. These values are quite high relative to several other monazites reported in the literature. As a comparison, the self-irradiation dose received by the well-studied Moacyr monazite (474 Ma) is $2.8\times10^{19}$ α-decay/g (2.3 dpa), $6.12\times10^{19}$ α-decay/g (5.13 dpa) for the Manangotry monazite from Madagascar (545 Ma) and $17\times10^{19}$ α-decay/g (14 dpa) for the old (1.9 Ga) monazite DIG19 from Devon Island (Seydoux-Guillaume et al., 2002c, 2004). Another monazite (1 Ga, 6 wt.% $ThO_2$ and 0.1 wt.% $UO_2$) from Norway (Nasdala et al., 2010) received a dose of $4.5\times10^{19}$ α-decay/g and is still crystalline. Such high doses must have been sufficient to totally amorphize all these monazites, because a dose of ca. $10^{19}$ α-decay/g is generally sufficient to completely amorphize solids (Weber et al., 1994). Since this is not the case for the monazites described herein, it must be concluded that they all have experienced annealing. As monazite is well-known to heal its radiation damage even at low temperature (Meldrum et al., 1997), thermal annealing provides an appropriate mechanism for the self-healing of the crystal structure contemporaneously with amorphization.

Since observations using TEM were also performed on altered monazites (Mnz2 from Ambato and Arendal), maximum self-irradiation

**Table 6**
U/Pb and Th/Pb data from LA-ICP-MS analyses of Sri Lanka monazite (altered monazite-Mnz2—in gray).

| # | Isotopic ratios | | | | | | | | Apparent ages (Ma) | | | | | | | | Concentration (ppm) | | |
|---|---|---|---|---|---|---|---|---|---|---|---|---|---|---|---|---|---|---|---|
| | $^{207}Pb/^{206}Pb$ | 2σ % | $^{207}Pb/^{235}U$ | 2σ % | $^{206}Pb/^{238}U$ | 2σ % | $^{208}Pb/^{232}Th$ | 2σ % | $^{207}Pb/^{206}Pb$ | 2σ | $^{207}Pb/^{235}U$ | 2σ | $^{206}Pb/^{238}U$ | 2σ | $^{208}Pb/^{232}Th$ | 2σ | Th | U | Th/U |
| 7 | 0.053 | 3.0 | 0.58 | 3.1 | 0.079 | 2.3 | 0.025 | 2.2 | 337 | 68 | 463 | 11 | 489 | 11 | 492 | 11 | 271,991 | 6696 | 41 |
| 8 | 0.055 | 3.1 | 0.61 | 3.2 | 0.080 | 2.3 | 0.024 | 2.1 | 414 | 69 | 483 | 12 | 498 | 11 | 485 | 10 | 248,251 | 6172 | 40 |
| 9 | 0.060 | 3.1 | 0.67 | 3.2 | 0.080 | 2.3 | 0.024 | 2.2 | 619 | 67 | 518 | 13 | 496 | 11 | 482 | 10 | 245,230 | 6099 | 40 |
| 10 | 0.054 | 3.1 | 0.60 | 3.2 | 0.080 | 2.3 | 0.024 | 2.2 | 360 | 70 | 475 | 12 | 499 | 11 | 489 | 10 | 243,913 | 6029 | 40 |
| 11 | 0.054 | 3.3 | 0.60 | 3.3 | 0.081 | 2.3 | 0.025 | 2.2 | 360 | 74 | 479 | 13 | 504 | 11 | 498 | 11 | 262,698 | 6398 | 41 |
| 12 | 0.054 | 3.1 | 0.59 | 3.2 | 0.079 | 2.3 | 0.025 | 2.2 | 357 | 69 | 469 | 12 | 492 | 11 | 492 | 11 | 259,164 | 6404 | 40 |
| 13 | 0.055 | 3.2 | 0.61 | 3.2 | 0.080 | 2.3 | 0.024 | 2.2 | 421 | 69 | 485 | 12 | 499 | 11 | 488 | 11 | 234,114 | 5878 | 40 |
| 14 | 0.054 | 3.1 | 0.61 | 3.2 | 0.082 | 2.3 | 0.025 | 2.2 | 369 | 69 | 484 | 12 | 509 | 11 | 497 | 11 | 229,442 | 5772 | 40 |
| 17 | 0.054 | 3.1 | 0.59 | 3.2 | 0.081 | 2.3 | 0.025 | 2.2 | 351 | 70 | 474 | 12 | 499 | 11 | 494 | 11 | 247,856 | 5980 | 41 |
| 18 | 0.055 | 3.3 | 0.61 | 3.3 | 0.080 | 2.3 | 0.025 | 2.2 | 398 | 71 | 481 | 13 | 499 | 11 | 490 | 11 | 222,658 | 5526 | 40 |
| 19 | 0.057 | 3.1 | 0.64 | 3.2 | 0.082 | 2.3 | 0.025 | 2.2 | 482 | 69 | 501 | 13 | 506 | 11 | 496 | 11 | 235,465 | 5780 | 41 |
| 20 | 0.057 | 3.3 | 0.63 | 3.3 | 0.080 | 2.3 | 0.025 | 2.2 | 486 | 73 | 495 | 13 | 497 | 11 | 496 | 11 | 233,714 | 5756 | 41 |
| 24 | 0.059 | 3.6 | 0.65 | 3.6 | 0.080 | 2.4 | 0.024 | 2.2 | 555 | 78 | 509 | 15 | 499 | 11 | 488 | 11 | 178,521 | 4180 | 43 |
| 29 | 0.063 | 3.4 | 0.70 | 3.4 | 0.081 | 2.4 | 0.025 | 2.2 | 710 | 71 | 540 | 15 | 500 | 11 | 493 | 11 | 215,482 | 5438 | 40 |
| 30 | 0.060 | 3.4 | 0.72 | 3.5 | 0.086 | 2.4 | 0.026 | 2.2 | 616 | 74 | 550 | 14 | 534 | 12 | 516 | 11 | 218,898 | 5230 | 42 |
| 31 | 0.060 | 3.6 | 0.65 | 3.7 | 0.079 | 2.4 | 0.024 | 2.2 | 594 | 78 | 510 | 24 | 492 | 11 | 475 | 10 | 261,113 | 6297 | 41 |
| 33 | 0.056 | 3.6 | 0.61 | 3.7 | 0.079 | 2.4 | 0.024 | 2.2 | 449 | 79 | 482 | 15 | 489 | 11 | 487 | 11 | 219,193 | 5261 | 42 |
| 34 | 0.061 | 3.5 | 0.70 | 3.5 | 0.082 | 2.4 | 0.025 | 2.2 | 645 | 74 | 536 | 51 | 511 | 12 | 489 | 11 | 245,670 | 5956 | 41 |
| 21 | 0.409 | 5.8 | 12.12 | 5.1 | 0.215 | 4.0 | 0.023 | 2.2 | 3943 | 86 | 2614 | 26 | 1255 | 46 | 455 | 10 | 54,801 | 50 | 1087 |
| 22 | 0.147 | 4.2 | 1.83 | 4.1 | 0.090 | 2.7 | 0.023 | 2.2 | 2316 | 71 | 1055 | 48 | 555 | 14 | 451 | 10 | 98,300 | 1394 | 71 |
| 23 | 0.063 | 6.1 | 0.74 | 5.9 | 0.085 | 2.8 | 0.024 | 2.2 | 698 | 127 | 561 | 14 | 528 | 14 | 483 | 11 | 80,546 | 983 | 82 |
| 27 | 0.456 | 6.1 | 19.43 | 1.0 | 0.309 | 4.4 | 0.022 | 2.2 | 4105 | 88 | 3064 | 59 | 1737 | 67 | 439 | 10 | 54,352 | 47 | 1145 |
| 28 | 0.087 | 12.6 | 0.93 | 0.1 | 0.078 | 4.9 | 0.022 | 2.3 | 1359 | 234 | 669 | 27 | 483 | 23 | 443 | 10 | 87,595 | 838 | 105 |
| 32* | 0.086 | 5.1 | 0.94 | 4.9 | 0.079 | 2.7 | 0.022 | 2.2 | 1329 | 97 | 671 | 15 | 492 | 13 | 435 | 10 | 153,383 | 2643 | 58 |

Location of analytical points (#) is in Fig. 2 (in red).
Th and U concentrations were calculated using Moacyr monazite standard.
#*: mixing with Mnz1.

doses were calculated for both crystals using the same ages as those of the unaltered monazites. Calculated doses are $2.4\times10^{19}$ α-decay/g (2.1 dpa) for Ambato and $4.7\times10^{19}$ α-decay/g (3.9 dpa) for Arendal. Both monazites (Arendal—Fig. 5a and Ambato—Fig. 5b) display very similar contrasts in TEM bright field images and have also very similar contrasts to previously studied monazites from Moss (Nasdala et al., 2010), Manangotry (Seydoux-Guillaume et al., 2004) and Moacyr (Seydoux-Guillaume et al., 2002c), which received similar doses ($4.5\times10^{19}$ α-decay/g, $2.8\times10^{19}$ α-decay/g, and $6.12\times10^{19}$ α-decay/g respectively). These results are in agreement with recrystallization occurring during the late stage of magma crystallization, but following Mnz1 growth (e.g. only few million years after).

### 7.3. Fluid-induced disturbance of U–Pb and Th–Pb geochronological systems

Poitrasson et al. (2000) have already emphasized the possibility of giving "a reasonable estimate of the age of the mineral–fluid interaction using the altered parts of the monazites". However in their case studies, except for one sample (M0111bis-Skiddaw granite), the compositions of the altered phases and alteration products were very different to that documented here (e.g. Th/U lower in altered monazites; Al and Ca involved). The present study has highlighted some important information related to the behavior of the U–Pb and Th–Pb geochronological systems with respect to low temperature (<320 °C—see above) hydrothermal alteration. The first one concerns the evolution of the Th/U ratio during alteration of monazite. Excluding the analyses clearly disturbed by thorite or Mnz1 contamination (i.e. #48, 49 and 59 for Ambato; #31 for Arendal or #32 for Sri Lanka), correlations between $^{208}Pb/^{232}Th$ ages and Th/U ratios (Fig. 10) during alteration of monazite (Mnz1 => Mnz2) demonstrate that Th/U ratios systematically increase with alteration. This is attributed to the higher solubility of U (as uranyl ions) in oxidized geological fluids (Mathieu et al., 2001). The observation that U is lost during the reaction, when mass balance is calculated for other elements, is in agreement with this interpretation. Th/U fractionation during monazite alteration has crucial consequences for the U–Pb and Th–Pb geochronological systems, as shown in Th–Pb Concordia diagrams in the cases of the Sri Lanka and the Arendal monazite samples (Fig. 9b and f). For both monazite samples, the U–Pb systems are affected by alteration (Tables 6 and 8). In the case of the Sri Lanka monazite (Fig. 9a) the Tera Wasserburg diagram demonstrates considerable common-Pb contamination (up to ~40% common-Pb). Combination of $^{206}Pb/^{238}U$ ratios with Th/U ratios indicates preferential loss of U. In the Arendal monazite, ages of the altered domains are scattered, but plot on the concordia curve of the TW diagram. These U–Pb ages are older than the age of the pristine domains, and hence are meaningless. Disturbance in U–Pb results is interpreted to arise from contamination by inherited Pb, but this is not clear in the TW diagram (certainly due to the analytical uncertainties). This shows that possible U–Pb disturbances cannot be ruled out even in cases in which the U–Pb data are concordant. In the case of geochronological studies based on large U–Pb datasets with no petrological control (as, for example, in provenance studies; e.g. Hietpas et al., 2010), similar U–Pb disturbances caused by later-stage low-grade hydrothermal alteration will be therefore hard to identify. In contrast, the $^{208}Pb/^{232}Th$ system in the altered domains gives ages ($450\pm18$ Ma for Sri Lanka and $864\pm21$ Ma for Arendal) that appear to be reasonable and are consistent with the alteration occurring soon after the magmatic crystallization of the Sri Lanka ($491\pm4$ Ma) and Arendal ($900\pm11$ Ma) monazites. Moreover, combination of Th/U ratios with these $^{208}Pb/^{232}Th$ ages (Fig. 10) helps to trace alteration events and increase the confidence in these alteration ages.

The behavior of the geochronological systems in the Ambato monazite in response to alteration contrasts with that of the other monazites. In this case both Th–Pb and U–Pb systems were affected. First, analyses within altered monazites exhibit strong common-Pb contamination ($^{207}Pb/^{206}Pb$ ratios enhanced; up to ~80% common-Pb in altered zones—Fig. 9c) leading to the disturbance of both U–Pb systems

**Table 7**
U/Pb and Th/Pb data from LA-ICP-MS analyses of Ambato monazite (altered monazite-Mnz2—in gray).

| # | Isotopic ratios | | | | | | | | Apparent ages (Ma) | | | | | | | | Concentration (ppm) | | |
|---|---|---|---|---|---|---|---|---|---|---|---|---|---|---|---|---|---|---|---|
| | $^{207}Pb/^{206}Pb$ | 2σ % | $^{207}Pb/^{235}U$ | 2σ % | $^{206}Pb/^{238}U$ | 2σ % | $^{208}Pb/^{232}Th$ | 2σ % | $^{207}Pb/^{206}Pb$ | 2σ | $^{207}Pb/^{235}U$ | 2σ | $^{206}Pb/^{238}U$ | 2σ | $^{208}Pb/^{232}Th$ | 2σ | Th | U | Th/U |
| 38 | 0.054 | 3.6 | 0.63 | 3.6 | 0.084 | 2.4 | 0.026 | 2.2 | 371 | 40 | 495 | 7 | 522 | 6 | 521 | 6 | 169,768 | 4953 | 34 |
| 39 | 0.054 | 3.6 | 0.63 | 3.6 | 0.084 | 2.4 | 0.025 | 2.3 | 389 | 39 | 497 | 7 | 520 | 6 | 508 | 6 | 170,436 | 4987 | 34 |
| 40 | 0.053 | 3.9 | 0.59 | 3.9 | 0.080 | 2.5 | 0.024 | 2.2 | 346 | 43 | 472 | 7 | 498 | 6 | 482 | 5 | 184,878 | 5704 | 32 |
| 41 | 0.055 | 3.6 | 0.63 | 3.7 | 0.084 | 2.4 | 0.026 | 2.3 | 394 | 40 | 499 | 7 | 522 | 6 | 512 | 6 | 170,013 | 5233 | 32 |
| 43 | 0.054 | 3.6 | 0.62 | 3.6 | 0.084 | 2.4 | 0.026 | 2.2 | 353 | 40 | 489 | 7 | 519 | 6 | 515 | 6 | 161,171 | 5899 | 27 |
| 44 | 0.055 | 3.6 | 0.63 | 3.7 | 0.083 | 2.4 | 0.026 | 2.3 | 404 | 40 | 496 | 7 | 517 | 6 | 510 | 6 | 145,147 | 5619 | 26 |
| 45 | 0.053 | 3.6 | 0.62 | 3.7 | 0.084 | 2.5 | 0.025 | 2.3 | 346 | 41 | 488 | 7 | 519 | 6 | 508 | 6 | 160,315 | 5967 | 27 |
| 48* | 0.085 | 4.1 | 0.96 | 4.1 | 0.082 | 2.6 | 0.025 | 2.3 | 1306 | 39 | 681 | 10 | 508 | 6 | 493 | 5 | 134,111 | 2851 | 47 |
| 49* | 0.083 | 3.6 | 0.99 | 3.6 | 0.086 | 2.5 | 0.026 | 2.2 | 1275 | 35 | 700 | 9 | 535 | 6 | 517 | 6 | 152,581 | 96228 | 2 |
| 50 | 0.054 | 3.8 | 0.63 | 3.8 | 0.084 | 2.5 | 0.025 | 2.3 | 381 | 42 | 495 | 7 | 519 | 6 | 508 | 6 | 144,983 | 5674 | 26 |
| 51 | 0.054 | 4.0 | 0.62 | 4.0 | 0.084 | 2.5 | 0.025 | 2.3 | 370 | 44 | 492 | 8 | 518 | 6 | 508 | 6 | 139,235 | 5057 | 28 |
| 52 | 0.054 | 4.0 | 0.60 | 4.0 | 0.080 | 2.5 | 0.025 | 2.3 | 374 | 44 | 476 | 8 | 498 | 6 | 507 | 6 | 140,609 | 4089 | 34 |
| 53 | 0.054 | 3.9 | 0.61 | 4.0 | 0.082 | 2.5 | 0.025 | 2.2 | 352 | 44 | 481 | 8 | 509 | 6 | 500 | 6 | 145,882 | 5616 | 26 |
| 58 | 0.696 | 3.6 | 49.50 | 3.6 | 0.516 | 2.5 | 0.046 | 2.2 | 4722 | 25 | 3982 | 18 | 2683 | 27 | 903 | 10 | 142,294 | 3952 | 36 |
| 59 | 0.703 | 3.7 | 9.64 | 3.7 | 0.099 | 2.5 | 0.015 | 2.3 | 4737 | 26 | 2401 | 17 | 611 | 7 | 294 | 3 | 223,407 | 8375 | 27 |
| 60 | 0.771 | 3.6 | 80.39 | 3.7 | 0.757 | 2.5 | 0.042 | 2.2 | 4869 | 26 | 4467 | 18 | 3632 | 35 | 828 | 9 | 101,930 | 1879 | 54 |
| 61 | 0.262 | 3.9 | 6.88 | 3.9 | 0.190 | 2.6 | 0.027 | 2.3 | 3261 | 31 | 2096 | 17 | 1123 | 13 | 540 | 6 | 87,778 | 1265 | 69 |
| 62 | 0.793 | 3.7 | 149.76 | 3.7 | 1.371 | 2.5 | 0.047 | 2.2 | 4908 | 26 | 5093 | 19 | 5565 | 46 | 920 | 10 | 183,144 | 2035 | 90 |
| 63 | 0.767 | 3.7 | 84.73 | 3.8 | 0.801 | 2.5 | 0.052 | 2.2 | 4862 | 26 | 4520 | 19 | 3794 | 35 | 1022 | 11 | 162,464 | 3247 | 50 |
| 64 | 0.696 | 3.7 | 54.70 | 3.8 | 0.571 | 2.5 | 0.047 | 2.2 | 4722 | 27 | 4082 | 19 | 2910 | 29 | 935 | 10 | 147,973 | 3864 | 38 |
| 65 | 0.719 | 3.8 | 62.06 | 3.8 | 0.626 | 2.5 | 0.047 | 2.3 | 4770 | 27 | 4208 | 19 | 3133 | 31 | 923 | 10 | 153,133 | 3215 | 48 |

Location of analytical points (#) is in Fig. 3 (in red). #*: analytical points in unaltered monazite but close to a crack.
Th and U concentrations were calculated using Moacyr monazite standard.
# 59: near thorium silicate inclusion.

(increases in $^{206}Pb/^{238}U$ and $^{207}Pb/^{235}U$ ratios and corresponding ages: Table 7 and Figs. 9c and 10b), and the Th–Pb system (increases in $^{208}Pb/^{232}Th$ ratios and corresponding ages: Table 7 and Figs. 9d and 10b), due to $^{208}Pb$ enhancement (Table 7 and Fig. 9d). Furthermore, in addition to common Pb contamination, evidence of (Th, U)-silicate contamination is provided by comparing the Th and U concentrations obtained by LA-ICP-MS (Table 7) with the concentrations obtained by EPMA analyses (Table 1). Both Th and U concentrations (LA-ICP-MS) are higher than the concentrations measured with EPMA (Table 1). This can be easily explained, firstly by the presence of many nano-fractures filled with Th–U-silicate (e.g. like analyses in Table 2) that may not be visible with SEM because of their size and their position under the surface (Fig. 5). Secondly, because the volumes analyzed by LA-ICP-MS (~50 $\mu m^3$) are at least 10 times larger than those measured by EPMA (max. 5 $\mu m^3$); the probability of producing mixed analyses (monazite + Th, U-silicate) through incorporation of high proportions of "unexpected" phases in the measured volume, is significantly higher in the case of LA-ICP-MS analyses.

The possibility of common-Pb contamination and chemical fractionation between Th and U has consequences for the interpretation or choice of analytical method used for dating. In the case of the Sri Lanka or the Arendal monazite samples, the common-Pb contaminations are relatively

**Table 8**
U/Pb and Th/Pb data from LA-ICP-MS analyses of Arendal monazite (altered monazite-Mnz2—in gray).

| # | Isotopic ratios | | | | | | | | Apparent ages (Ma) | | | | | | | | Concentration (ppm) | | |
|---|---|---|---|---|---|---|---|---|---|---|---|---|---|---|---|---|---|---|---|
| | $^{207}Pb/^{206}Pb$ | 2σ % | $^{207}Pb/^{235}U$ | 2σ % | $^{206}Pb/^{238}U$ | 2σ % | $^{208}Pb/^{232}Th$ | 2σ % | $^{207}Pb/^{206}Pb$ | 2σ | $^{207}Pb/^{235}U$ | 2σ | $^{206}Pb/^{238}U$ | 2σ | $^{208}Pb/^{232}Th$ | 2σ | Th | U | Th/U |
| 7 | 0.065 | 2.9 | 1.38 | 3.0 | 0.153 | 2.4 | 0.047 | 2.3 | 775 | 30 | 879 | 9 | 920 | 10 | 928 | 10 | 108,793 | 6093 | 18 |
| 8 | 0.065 | 2.8 | 1.39 | 3.0 | 0.154 | 2.4 | 0.046 | 2.3 | 789 | 30 | 883 | 9 | 922 | 10 | 913 | 10 | 113,231 | 6264 | 18 |
| 9 | 0.065 | 2.9 | 1.38 | 3.0 | 0.153 | 2.4 | 0.047 | 2.2 | 786 | 30 | 882 | 9 | 920 | 10 | 922 | 10 | 109,113 | 5961 | 18 |
| 10 | 0.066 | 2.9 | 1.35 | 3.0 | 0.149 | 2.4 | 0.046 | 2.2 | 797 | 30 | 866 | 9 | 894 | 10 | 905 | 10 | 108,089 | 6224 | 17 |
| 11 | 0.066 | 3.0 | 1.38 | 3.1 | 0.152 | 2.4 | 0.046 | 2.2 | 800 | 32 | 880 | 9 | 912 | 10 | 918 | 10 | 88,006 | 4819 | 18 |
| 12 | 0.066 | 2.9 | 1.38 | 3.0 | 0.153 | 2.4 | 0.046 | 2.2 | 790 | 30 | 881 | 9 | 917 | 10 | 918 | 10 | 105,997 | 6120 | 17 |
| 13 | 0.066 | 3.0 | 1.37 | 3.1 | 0.150 | 2.4 | 0.046 | 2.3 | 804 | 31 | 875 | 9 | 904 | 10 | 911 | 10 | 108,499 | 6304 | 17 |
| 14 | 0.068 | 3.2 | 1.49 | 3.3 | 0.159 | 2.4 | 0.044 | 2.3 | 866 | 33 | 925 | 10 | 950 | 11 | 861 | 9 | 103,658 | 5179 | 20 |
| 17 | 0.066 | 2.9 | 1.35 | 3.1 | 0.149 | 2.4 | 0.045 | 2.2 | 805 | 31 | 870 | 9 | 895 | 10 | 899 | 10 | 58,119 | 6507 | 9 |
| 18 | 0.066 | 3.0 | 1.35 | 3.1 | 0.148 | 2.4 | 0.045 | 2.3 | 810 | 31 | 868 | 9 | 890 | 10 | 895 | 10 | 64,163 | 5971 | 11 |
| 19 | 0.065 | 3.0 | 1.34 | 3.1 | 0.149 | 2.4 | 0.045 | 2.2 | 790 | 32 | 864 | 9 | 893 | 10 | 883 | 10 | 57,555 | 5950 | 10 |
| 20 | 0.065 | 3.1 | 1.33 | 3.2 | 0.149 | 2.4 | 0.044 | 2.2 | 758 | 32 | 858 | 9 | 897 | 10 | 866 | 10 | 60,001 | 5598 | 11 |
| 21 | 0.065 | 3.1 | 1.34 | 3.2 | 0.148 | 2.4 | 0.045 | 2.2 | 785 | 32 | 861 | 9 | 891 | 10 | 883 | 10 | 56,738 | 5731 | 10 |
| 22 | 0.066 | 3.0 | 1.34 | 3.1 | 0.147 | 2.4 | 0.045 | 2.2 | 811 | 31 | 862 | 9 | 882 | 10 | 898 | 10 | 62,638 | 6662 | 9 |
| 23 | 0.065 | 3.1 | 1.35 | 3.1 | 0.150 | 2.4 | 0.045 | 2.2 | 788 | 32 | 867 | 9 | 898 | 10 | 898 | 10 | 54,275 | 6035 | 9 |
| 24 | 0.066 | 3.0 | 1.39 | 3.1 | 0.153 | 2.4 | 0.046 | 2.2 | 801 | 31 | 886 | 9 | 920 | 10 | 915 | 10 | 59,178 | 6569 | 9 |
| 28 | 0.070 | 8.2 | 1.55 | 8.0 | 0.161 | 3.4 | 0.044 | 2.3 | 929 | 82 | 951 | 25 | 960 | 15 | 871 | 10 | 57,422 | 185 | 311 |
| 29 | 0.070 | 9.3 | 1.45 | 9.0 | 0.150 | 3.6 | 0.044 | 2.2 | 930 | 92 | 910 | 27 | 902 | 15 | 866 | 10 | 61,608 | 169 | 365 |
| 30 | 0.073 | 7.8 | 1.73 | 7.6 | 0.173 | 3.3 | 0.044 | 2.2 | 1000 | 77 | 1018 | 24 | 1027 | 16 | 871 | 10 | 59,815 | 157 | 380 |
| 31* | 0.067 | 3.5 | 1.43 | 3.6 | 0.154 | 2.5 | 0.047 | 2.3 | 851 | 36 | 903 | 11 | 924 | 11 | 929 | 10 | 86,696 | 3266 | 27 |
| 33 | 0.075 | 11.9 | 1.792 | 11.5 | 0.173 | 4.3 | 0.044 | 2.3 | 1076 | 115 | 1043 | 38 | 1027 | 21 | 879 | 10 | 50,132 | 83 | 603 |
| 34 | 0.081 | 9.5 | 2.29 | 9.2 | 0.205 | 3.9 | 0.042 | 2.3 | 1218 | 90 | 1208 | 32 | 1203 | 21 | 837 | 9 | 63,898 | 133 | 479 |

Location of analytical points (#) is in Fig. 4 (in red). Mnz1 from 7 to 14; Mnz1′ from 17 to 24 and Mnz2 from 28 to 34.
Th and U concentrations were calculated using Moacyr monazite standard.
#*:mixed with Mnz1.

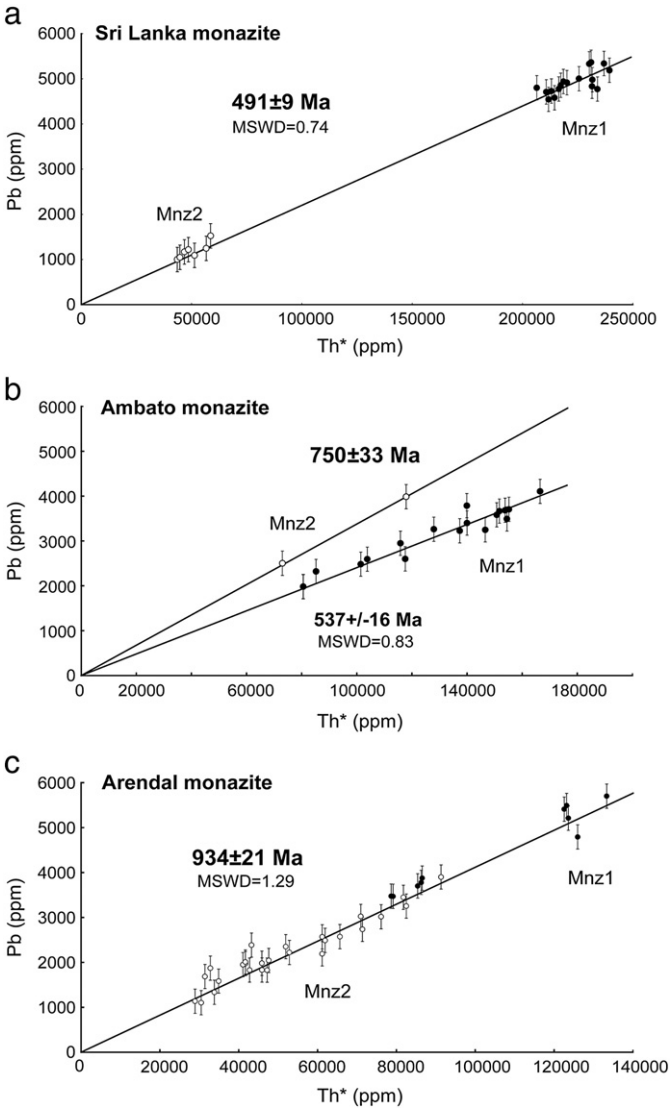


**Fig. 8.** EPMA chemical Th equivalent—total Pb pseudo-isochron (after Suzuki and Adachi, 1991) for Sri Lanka (a), Arendal (b) and Ambato (c) monazites. In the Sri Lanka and Ambato monazite samples, the ages for both pristine (Mnz1) and altered (Mnz2) zones are statistically similar. For Ambato monazite, ages from the altered zones are significantly older (750 Ma): see discussion in text. Ages were calculated following Montel et al. (1996).

low, i.e. only visible on the $^{206}$Pb and $^{207}$Pb signals, but not in $^{208}$Pb. As a result, only the U–Pb systems have been noticeably affected. Chemical dating by EPMA, which uses total Pb for analyses, i.e. essentially $^{208}$Pb for monazite, therefore remains unaffected by the common-Pb contamination and yields ages consistent with LA-ICP-MS. LA-ICP-MS dating, on the other hand, allows a consistent estimation of the alteration age to be obtained since it is only a few million years younger that the initial age. EPMA dating cannot distinguish between these ages due to the significantly lower precision of this method (Fig. 8). The combination of Th–Pb dating (LA-ICP-MS) with Th/U ratios, increases in which provide evidence for hydrothermal alteration, gives a powerful tool to estimate the age of alteration, provided the monazites are carefully characterized previously by methods such as SEM and TEM. Finally, if the Th–Pb and U–Pb systems are both disturbed (Ambato monazite), and if common-Pb contamination is so high that even $^{208}$Pb is affected, both analytical techniques (LA-ICP-MS and EPMA) do not allow the alteration age to be discriminated and quantified. However, careful analyses with these methods coupled with meticulous analyses with SEM and TEM allow alteration events to be traced and the disturbance of the geochronological systems applied as well as element mobility to be evaluated.

## 8. Conclusions

This investigation of large (cm) single monazite crystals from three distinct pegmatite localities allows the following important, more general, conclusions to be drawn.

1- The typical alteration of a primary (Mnz1) high-temperature monazite by a fluid at moderate temperature (<320 °C) results in the formation of Th(Y)-depleted monazite (Mnz2) in association with Th-rich phases (thorium silicate or thorium oxide) ± Y-xenotime. The resulting Mnz2 monazite always displays a higher Th/U ratio than the primary monazite, due to a fractionation of U relative to Th during the alteration process, which itself could be a good signature to trace the presence of hydrothermal alteration.

2- Alteration textures are always associated with radial cracks emanating from highly radioactive microscopic phases (thorium silicate or thorium oxide) present in the altered domains. The networks of fractures, interpreted to be caused by radiation-damage induced swelling of the radioactive phases, may facilitate the circulation of fluids, which can then mobilize and carry dissolved elements (e.g. Fe, Th, Pb, U) away.

3- Attempts to date alteration using electron probe chemical dating have not been successful, because the age difference between the original monazite and its alteration products in each case is well within the accuracy of the technique. In one case, the altered monazite (Ambato) is so contaminated by common-Pb that it also affected by the amount of $^{208}$Pb, so that the total Pb measured by EPMA is higher than it should be. In this case, dates obtained in the altered zones are anomalously old and meaningless. However, chemical U–Th–Pb ages obtained for primary and pristine monazites are in agreement with LA-ICP-MS dating.

4- It is possible to produce indicative ages for alteration using high-resolution (5 μm) U–Pb and Th–Pb dating with the LA-ICP-MS technique. This is only possible when the altered zones are not too contaminated by common-Pb and contain few nano-phases or nano-c racks filled with Th-rich phases (case of Ambato monazite). Under these conditions, the Th–Pb system has been shown to be more reliable than the U–Pb systems, because of the preferential loss of U and the high Th contents (and hence high radiogenic $^{208}$Pb) in even the altered monazite.

5- The combination of Th–Pb dating (LA-ICP-MS) with Th/U ratios, which can be used as evidence for hydrothermal alteration, provides a powerful tool for discriminating and estimating monazite alteration ages. However, it must be emphasized that even careful microscopic (SEM) characterization of the monazites may be not sufficient to achieve this goal, since nano-phases only observable by TEM (e.g. Ambato monazite), may influence the Th–Pb isotopic system and hence lead to disturbed and meaningless ages.

## Acknowledgments

We are indebted to Thorsten Geisler (Univ. Bonn), Michel Guiraud and Benjamin Rondot (Museum National d'Histoire Naturelle de Paris) for providing of the monazite samples. Collaborations were promoted thanks to PHC Aurora and Procope programs (Ministry of Foreign affairs) and thanks to funding from University Paul Sabatier (BB spent two months as invited professor in Toulouse). The authors want to thank Simon Harley for checking both the scientific and the English content of this paper. Comments by N. Kelly, P. Tropper, an anonymous reviewer and the Editor-in-Chief K. Mezger were appreciated. This study was supported by both CNRS-INSU and a PCR GUTEC.

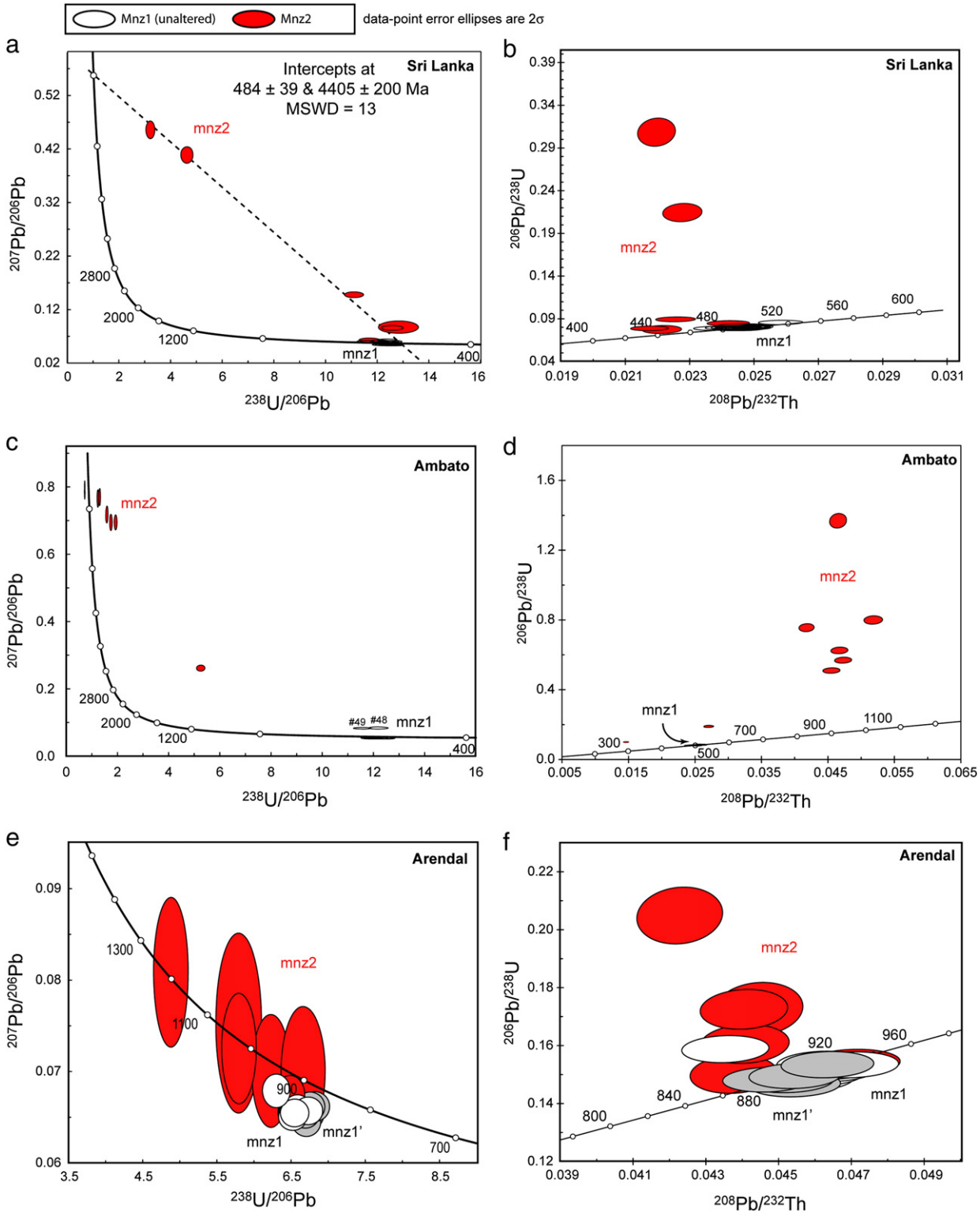


**Fig. 9.** Tera Wasserburg ($^{207}Pb/^{206}Pb$ vs $^{238}U/^{206}Pb$) and $^{206}Pb/^{238}U$ vs $^{208}Pb/^{232}Th$ modified concordia diagrams with analyses obtained by laser ablation inductively coupled plasma spectrometry (LA-ICP-MS) for each monazite: Sri Lanka (a–b), Ambato (c–d) and Arendal (e–f)—see Tables 6–8 and locations in Figs. 2–4. Data-point error ellipses are 2σ, red filled ellipses correspond to altered monazites (Mnz2) and white (Mnz1) or light gray filled ellipses (Mnz1′) for pristine zones. For the Sri Lanka-Mnz1, the weighted $^{206}Pb/^{238}U$ mean (WM) age is 500 ± 5 Ma [MSWD = 3.1; n = 18] and 491 ± 4 Ma [MSWD = 2.4; n = 18] for the WM $^{208}Pb/^{232}Th$ age. In the case of the Ambato-Mnz1, the WM $^{206}Pb/^{238}U$ age is 514 ± 6 Ma [MSWD = 9; n = 11] and 507 ± 7 Ma [MSWD = 13; n = 11] for WM $^{208}Pb/^{232}Th$ age. Finally, for the Arendal-Mnz(1 + 1′), the pooled WM $^{206}Pb/^{238}U$ age is 906 ± 9 Ma [MSWD = 11.6; n = 16] and the pooled WM $^{208}Pb/^{232}Th$ age is 900 ± 11 Ma [MSWD = 16; n = 16]. See details in the text.

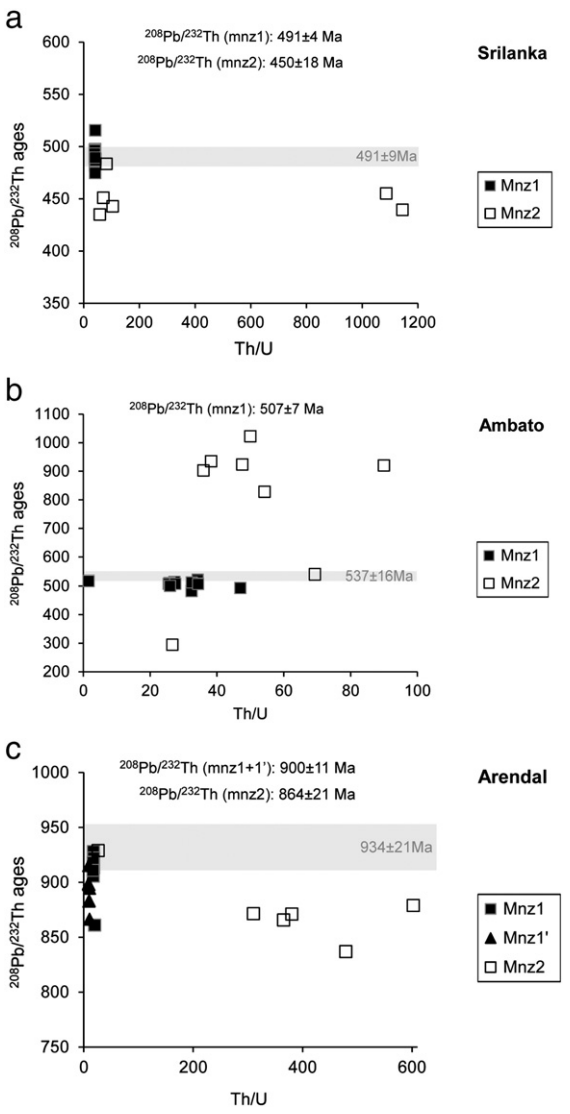


**Fig. 10.** $^{232}Th/^{208}Pb$ ages vs Th/U ratios in pristine and altered zones of the Sri Lanka (a), Ambato (b) and Arendal (c) monazite samples. Data points and errors for ages are in Tables 6 to 8, Th/U ratios are in Table 1.

## References


Ancey, M., Bastenaire, F., Tixier, R., 1978. Application des méthodes statistiques en microanalyse. In: Maurice, F., Meny, L., Tixier, R. (Eds.), Microanalyse, microscopie electronique à balayage. Les Editions du Physicien, Orsay, France, pp. 323–347.

Berger, A., Gnos, E., Janots, E., Fernandez, A., Giese, J., 2008. Formation and composition of rhabdophane, bastnäsite and hydrated thorium minerals during alteration: implications for geochronology and low-temperature processes. Chemical Geology 254, 238–248.

Bilal, E., Marciano, V., Neves, J.M.C., Fuzikawa, K., Riffel, B.F., Nalini, H.A., Fernandes, M.L., Nasraoui, M., 1998. Hydrothermal alteration of monazite-(Ce) from the Santa Maria de Itabira pegmatite district (Minas Gerais, Brazil). Comptes Rendus de l' Academie des Sciences 326, 693–700.

Black, L.P., Fitzgerald, J.D., Harley, S.L., 1984. Pb isotopic composition, colour, and microstructure of monazites from a polymetamorphic rock in Antarctica. Contributions to Mineralogy and Petrology 85, 141–148.

Bosse, V., Boulvais, P., Gautier, P., Tiepolo, M., Ruffet, G., Devidal, J.L., Cherneva, Z., Gerdjikov, I., Paquette, J.L., 2009. Fluid-induced disturbance of the monazite Th–Pb chronometer: in situ dating and element mapping in pegmatites from the Rhodope (Greece, Bulgaria). Chemical Geology 261, 286–302.

Budzyn, B., Hetherington, C.J., Williams, M.L., Jercinovic, M.J., Michalik, M., 2010. Fluid–mineral interactions and constraints on monazite alteration during metamorphism. Mining Magazine 74, 659–681.

Castaing, R., 1960. Advances in Electronics and Electron Physics, vol. 13. Academic Press, New York, N.Y.

Cherniak, D.J., 2010. Diffusion in accessory minerals zircon, titanite, apatite, monazite and xenotime. In: Zhang, Y.X., Cherniak, D.J. (Eds.), Rev. Mineral. Geochem., 72. Mineral. Soc. Amer., Washington DC, pp. 827–869.

Cherniak, D.J., Pyle, J.M., 2008. Th diffusion in monazite. Chemical Geology 256, 52–61.

Cherniak, D.J., Watson, E.B., Grove, M., Harrison, T.M., 2004. Pb diffusion in monazite: a combined RBS/SIMS study. Geochimica et Cosmochimica Acta 68, 829–840.

Cuney, M., Mathieu, R., 2000. Extreme light rare earth element mobilization by diagenetic fluids in the geological environment of the Oklo natural reactor zones, Franceville basin, Gabon. Geology 28, 743–746.

Devidal, J.L., Gibert, F., Kieffer, B., Pin, C., Montel, J.M., 1998. A new method for solubility measurement: application to $NdPO_4$ system in $H_2O$–NaCl–HCl hydrothermal fluids. Mining Magazine 62A, 375–376.

Didier, A., Bosse, V., Bouloton, J., Boulvais, P., Paquette, J.-L., Montel, J.-M., 2011. Fluid-induced disturbance of the U–Th–Pb chronometers in monazite: LA-ICP-MS in-situ dating study in microgranites (Velay, France). GSA Annual Meeting Minneapolis Minnesota.

Evron, R., Kimmel, G., Eyal, Y., 1994. Thermal recovery of self-radiation damage in uraninite and thorianite. Journal of Nuclear Materials 217, 54–66.

Ewing, R.C., 1994. The metamict state: 1993—the centennial. Nuclear Instruments and Methods in Physics Research B91, 22–29.

Ewing, R.C., Weber, W.J., Clinard Jr., F.W., 1995. Radiation effects in nuclear waste forms. Progress in Nuclear Energy 29, 63–127.

Ewing, R.C., Meldrum, A., Wang, L.M., Wang, S.X., 2000. Radiation-induced amorphisation. In: Ribbe, P.H. (Ed.), Reviews in Mineralogy and Geochemistry, 39. Mineral. Soc. Amer., Washington DC, pp. 319–361.

Farges, F., Calas, G., 1991. Structural analysis of radiation damage in zircon and thorite: an X-ray absorption spectroscopic study. American Mineralogist 76, 60–73.

Finger, F., Broska, I., Roberts, M.P., Schermaier, A., 1998. Replacement of primary monazite by apatite-allanite-epidote coronas in an amphibolite facies granite gneiss from the eastern Alps. American Mineralogist 83, 248–258.

Förster, H.J., 1998. The chemical composition of REE-Y–Th–U-rich accessory minerals in peraluminous granites of the Erzgebirge-Fichtelgebirge region, Germany, Part I: the monazite–(Ce)–brabantite solid solution series. American Mineralogist 83, 259–272.

Franz, G., Andrehs, G., Rhede, D., 1996. Crystal chemistry of monazite and xenotime from Saxothuringian-Moldanubian metapelites, NE Bavaria, Germany. European Journal of Mineralogy 8, 1097–1118.

Friedrich, M.H., Cuney, M., Poty, B., 1987. Uranium geochemistry in peraluminous leucogranites. Uranium 3, 353–385.

Gardés, E., Jaoul, O., Montel, J.-M., Seydoux-Guillaume, A.-M., Wirth, R., 2006. Pb diffusion in monazite: an experimental study of the $Pb^{2+}+Th^{4+}$ $2Nd^{3+}$ interdiffusion. Geochimica et Cosmochimica Acta 70, 2325–2336.

Gardès, E., Montel, J.-M., Seydoux-Guillaume, A.M., Wirth, R., 2007. Pb diffusion in monazite: new constraints from the experimental study of $Pb^{2+}$ $Ca^{2+}$ interdiffusion. Geochimica et Cosmochimica Acta 71, 4036–4043.

Gasquet, D., Bertrand, J.M., Paquette, J.L., Lehmann, J., Ratzov, G., De Ascenção, Guedes R., Tiepolo, M., Boullier, A.M., Scaillet, S., Nomade, S., 2010. Miocene to Messinian deformation and hydrothermalism in the Lauzière Massif (French Western Alps): new U–Th–Pb and Argon ages. Bulletin de la Société Géologique de France 181, 227–241.

Gratz, R., Heinrich, W., 1997. Monazite–xenotime thermobarometry: experimental calibration of the miscibility gap in the binary system $CePO_4$–$YPO_4$. American Mineralogist 82, 772–780.

Harlov, D.E., Wirth, R., Hetherington, C.J., 2011. Fluid-mediated partial alteration in monazite: the role of coupled dissolution-reprecipitation in element redistribution and mass transfer). Contributions to Mineralogy and Petrology 162, 329–348.

Harrison, T.M., Catlos, E., Montel, J.M., 2002. U–Th–Pb dating of phosphate minerals. In: Ribbe, P.H. (Ed.), Rev. Mineral. Geochem., 48. Mineral. Soc. Amer., Washington DC, pp. 523–558.

Hay, D.C., Dempster, T.J., 2009. Zircon behaviour during low-temperature metamorphism. Journal of Petrology 50, 571–589.

Hecht, L., Cuney, M., 2000. Hydrothermal alteration of monazite in the Precambrian crystalline basement of the Athabasca Basin (Saskatchewan, Canada): implications for the formation of unconformity-related uranium deposits. Mineralium Deposita 35, 791–795.

Heinrich, W., Andrehs, G., Franz, G., 1997. Monazite–xenotime miscibility gap thermometry: I. An empirical calibration. Journal of Metamorphic Geology 15, 3–17.

Hetherington, C.J., Harlov, D.E., 2008. Metasomatic thorite and uraninite inclusions in xenotime and monazite from granitic pegmatites, Hidra anorthosite massif, southwestern Norway: mechanics and fluid chemistry. American Mineralogist 93, 806–820.

Hetherington, C.J., Harlov, D.E., Budzyn, B., 2010. Experimental metasomatism of monazite and xenotime: mineral stability, REE mobility and fluid composition. Mineralogy and Petrology 99, 165–184.

Hietpas, J., Samson, S., Moecher, D., Schmitt, A.K., 2010. Recovering tectonic events from the sedimentary record: detrital monazite plays in high fidelity. Geology 167–170.

Jackson, S.E., Pearson, N.J., Griffin, W.L., Belousova, E.A., 2004. The application of laser ablation-inductively coupled plasma-mass spectrometry to in situ U–Pb zircon geochronology. Chemical Geology 211, 47–69.

Janots, E., Engi, M., Rubatto, D., Berger, A., Gregory, C., Rahn, M., 2009. Metamorphic rates in collisional orogeny from in situ allanite and monazite dating. Geology 37, 11–14.

Janots, E., Berger, A., Engi, M., 2011. Physico-chemical control on the REE minerals in chloritoid-grade metasediments from a single outcrop (Central Alps, Switzerland). Lithos 121, 1–11.

Janots, E., Berger, A., Gnos, E., Whitehouse, M., Lewin, E., Pettke, T., 2012. Constraints on fluid evolution during metamorphism from U–Th–Pb systematics in Alpine clef-hosted monazite. Chemical Geology. http://dx.doi.org/10.1016/j.chemgeo.2012.07.014.

Jercinovic, M.J., Williams, M.L., 1999. Analytical perils (and progress) in electron microprobe trace element analysis applied to geochronology: background acquisition, interferences, and beam irradiation effects. American Mineralogist 90, 526–546.

Lee, J.K.W., Tromp, J., 1995. Self-induced fracture generation in zircon. Journal of Geophysical Research 100, 17753–17770.

Ludwig, K.R., 2001. User's manual for Isoplot/Ex Version 2.49, a geochronological toolkit for Microsoft Excel. Berkeley Geochronological Center, Spec Publ 1a, Berkeley, USA. 55 pp.

Lumpkin, G.R., Chakoumakos, B.C., 1988. Chemistry and radiation effects of thorite-group minerals from the Harding pegmatite, Taos County, New Mexico. American Mineralogist 73, 1405–1419.
Mathieu, R., Zetterström, L., Cuney, M., Gauthier-Lafaye, F., Hidaka, H., 2001. Alteration of monazite and zircon and lead migration as geochemical tracers of fluid paleocirculations around the Oklo-Okélobondo and Bangombé natural nuclear reactor zones (Franceville basin, Gabon). Chemical Geology 171, 147–171.
Meldrum, A., Boatner, L.A., Wang, L.M., Ewing, R.C., 1997. Displacive irradiation effects in the monazite- and zircon-structure orthophosphates. Physical Review B56, 13805–13814.
Meldrum, A., Boatner, L.A., Weber, W.J., Ewing, R.C., 1998. Radiation damage in zircon and monazite. Geochimica et Cosmochimica Acta 62, 2509–2520.
Montel, J.M., Foret, S., Veschambre, M., Nicollet, C., Provost, A., 1996. Electron microprobe dating of monazite. Chemical Geology 131, 37–53.
Montel, J.M., Razafimahatratra, D., Ralison, B., de Parseval, P., Thibault, M., Randranja, R., 2011. Monazite from mountain to ocean: a case study from Trolognaro (Fort-Dauphin), Madagascar. European Journal of Mineralogy 23, 745–757.
Müller, W., Shelley, M., Miller, P., Broude, S., 2009. Initial performance metrics of a new custom-designed ArF excimer LA-ICPMS system coupled to a two-volume laser-ablation cell. Journal of Analytical Atomic Spectrometry 24, 209–214.
Nasdala, L., Pidgeon, R.T., Wolf, D., 1996. Heterogeneous metamictization of zircon on a microscale. Geochimica et Cosmochimica Acta 60, 1091–1097.
Nasdala, L., Wenzel, M., Vavra, G., Irmer, G., Wenzel, T., Kober, B., 2001. Metamictisation of natural zircon: accumulation versus thermal annealing of radioactivity-induced damage. Contributions to Mineralogy and Petrology 141, 125–144.
Nasdala, L., Kronz, A., Wirth, R., Vaczi, T., Perez-Soba, C., Willner, A., Kennedy, A.K., 2009. The phenomenon of deficient electron microprobe totals in radiation-damaged and altered zircon. Geochimica et Cosmochimica Acta 73, 1637–1650.
Nasdala, L., Ruschel, K., Rhede, D., Wirth, R., Kerschhofer-Wallner, L., Kennedy, A.K., Kinny, P.D., Finger, F., Groschopf, N., 2010. Phase decomposition upon alteration of radiation-damaged monazite–(Ce) from Moss, Østfold, Norway. Chimia 64, 705–711.
Ni, Y., Hughes, J.M., Mariano, A.N., 1995. Crystal chemistry of the monazite and xenotime structures. American Mineralogist 80, 21–26.
Oelkers, E.H., Poitrasson, F., 2002. An experimental study of the dissolution stoichiometry and rates of a natural monazite as a function of temperature from 50 to 230°C and pH from 1.5 to 10. Chemical Geology 191, 73–87.
Ouchani, S., Dran, J.C., Chaumont, J., 1997. Evidence of ionization annealing upon helium-ion irradiation of pre-damaged fluorapatite. Nuclear Instruments and Methods in Physics Research Section B 132, 447–451.
Overwijk, M.H.F., van den Heuvel, F.C., Bulle-Lieuwma, C.W.T., 1993. Novel scheme for the preparation of transmission electron microscopy specimens with a focused ion beam. Journal of Vacuum Science and Technology 11, 202.
Pabst, A., 1952. The metamict state. American Mineralogist 37, 137–157.
Paquette, J.L., Tiepolo, M., 2007. High resolution (5 μm) U–Th–Pb isotopes dating of monazite with excimer laser ablation (ELA)-ICPMS. Chemical Geology 240, 222–237.
Parrish, R.R., 1990. U–Pb dating of monazite and its application to geological problems. Canadian Journal of Earth Sciences 27, 1431–1450.
Picot, V., Deschanels, X., Peuget, S., Glorieux, G., Seydoux−Guillaume, A.M., Wirth, R., 2008. Ion Beam Radiation Effects in Monazite. Journal of Nuclear Materials 381, 290–296.
Poitrasson, F., Chenery, S., Bland, D.J., 1996. Contrasted monazite hydrothermal alteration mechanisms and their geochemical implications for the U–Th–Pb geochronology and nuclear ceramics. Earth and Planetary Science Letters 145, 79–96.
Poitrasson, F., Chenery, S., Shepherd, T.J., 2000. Electron microprobe and LA-ICP-MS study of monazite hydrothermal alteration: implications for the U–Th–Pb geochronology and nuclear ceramics. Geochimica et Cosmochimica Acta 64, 3283–3297.
Poitrasson, F., Oelkers, E., Schott, J., Montel, J.M., 2004. Experimental determination of synthetic $NdPO_4$ monazite end-member solubility in water from 21 degrees C to 300 degrees C: implications for rare earth element mobility in crustal fluids. Geochimica et Cosmochimica Acta 68, 2207–2221.
Pourtier, E., Devidal, J.L., Gibert, F., 2010. Solubility measurements of synthetic neodymium monazite as a function of temperature at 2 kbars, and aqueous neodymium speciation in equilibrium with monazite. Geochimica et Cosmochimica Acta 74, 1872–1891.
Putnis, A., 2009. Mineral replacement reactions. Reviews in Mineralogy and Geochemistry: Mineralogical Society of America, 70, pp. 87–124.
Roberts, S., McCaffrey, J., Giannuzzi, L., Stevie, F., Zaluzec, N., 2001. Advanced techniques in TEM specimen preparation. In: Zhang, Xiao-Feng, Zhang, Ze (Eds.), Progress in Transmission Electron Microscopy: Springer Series in Surface Sciences, 38, pp. 336–342.
Roy, P.S., 1999. Heavy mineral beach placers in Souheastern Australia: their nature and genesis. Economic Geology 94, 567–588.
Schmidt, C., Rickers, K., Bilderback, D.H., Huang, R., 2007. In situ synchrotron-radiation XRF study of REE phosphate dissolution in aqueous fluids to 800 degrees C. Lithos 95, 87–102.
Seydoux-Guillaume, A.M., Paquette, J.L., Wiedenbeck, M., Montel, J.M., Heinrich, W., 2002a. Experimental resetting of the U-Th-Pb system in monazite. Chemical Geology 191, 165–181.
Seydoux-Guillaume, A.M., Wirth, R., Heinrich, W., Montel, J.M., 2002b. Experimental determination of the Th partitioning between monazite and xenotime using Analytical Electron Microscopy and X-ray Diffraction Rietveld analysis. European Journal of Mineralogy 14, 869–878.
Seydoux-Guillaume, A.M., Wirth, R., Nasdala, L., Gottschalk, M., Montel, J.M., Heinrich, W., 2002c. An XRD, TEM and Raman study of experimentally annealed natural monazite. Physics and Chemistry of Minerals 29, 240–253.
Seydoux-Guillaume, A.M., Goncalves, P., Wirth, R., Deutsch, A., 2003. TEM study of polyphasic and discordant monazites: site specific specimen preparation using the Focused Ion Beam technique. Geology 31, 973–976.
Seydoux-Guillaume, A.M., Wirth, R., Deutsch, A., Schärer, U., 2004. Microstructure of 24–1928 Ma concordant monazites: implications for geochronology and nuclear waste deposits. Geochimica et Cosmochimica Acta 68, 2517–2527.
Seydoux-Guillaume, A.M., Wirth, R., Ingrin, J., 2007. Contrasting response of $ThSiO_4$ and monazite to natural irradiation. European Journal of Mineralogy 19, 7–14.
Seydoux-Guillaume, A.M., Montel, J.M., Wirth, R., Moine, B., 2009. Radiation damages in diopside and calcite crystals from uranothorianite inclusions. Chemical Geology 261, 318–332.
Spear, F.S., Pyle, J.M., 2002. Apatite, Monazite and Xenotime in metamorphic rocks. In: Ribbe, P.H. (Ed.), Rev. Mineral. Geochem., 48. Mineral. Soc. Amer., Washington DC, pp. 293–335.
Suzuki, K., Adachi, M., 1991. Precambrian provenance and Silurian metamorphism of the Tsubonosawa paragneiss in the South Kitakami terrane, Northeast Japan, revealed by the chemical Th–U–total Pb isochron ages of monazite, zircon and xenotime. Geochemical Journal 25, 357–376.
Teufel, S., Heinrich, W., 1997. Partial resetting of the U–Pb isotope system in monazite through hydrothermal experiments: an SEM and U–Pb isotope study. Chemical Geology 137, 273–281.
Tiepolo, M., 2003. In situ Pb geochronology of zircon with laser ablation-inductively coupled plasma-sector field mass spectrometry. Chemical Geology 141, 1–19.
Tropper, P., Manning, C.E., Harlov, C.E., 2011. Solubility of $CePO_4$ monazite and $YPO_4$ xenotime in $H_2O$ and $H_2O$–NaCl at 800 degrees C and 1 GPa: implications for REE and Y transport during high-grade metamorphism. Chemical Geology 282, 58–66.
van Achterbergh, E., Ryan, C.G., Jackson, S.E., Griffin, W., 2001. Data reduction software for LA-ICP-MS. In: Sylvester, P. (Ed.), Laser Ablation-ICPMS in the Earth Science: Mineralogical Association of Canada, vol. 29, pp. 239–243.
van Emden, B., Graham, J., Lincoln, F.G., 1997. The incorporation of actinides in monazite and xenotime from placer deposits in western Australia. The Canadian Mineralogist 35, 95–104.
Weber, W.J., Ewing, R.C., Wang, L.M., 1994. The radiation-induced crystalline-toamorphous transition in zircon. Journal of Materials Research 9, 688–698.
Weber, W.J., Ewing, R.C., Catlow, C.R.A., Diaz de la Rubia, T., Hobbs, L.W., Kinishita, C., Matzke, H.J., Motta, A.T., Nastasi, M., Salje, E.H.K., Vance, E.R., Zinkle, S.J., 1998. Radiation effects in crystalline ceramics for the immobilization of high-level nuclear waste and plutonium. Journal of Materials Research 13, 1434–1484.
Williams, M.L., Jercinovic, M.J., Harlov, D.E., Budzyn, B., Hetherington, C.J., 2011. Resetting monazite ages during fluid-related alteration. Chemical Geology 283, 218–225.
Wirth, R., 2004. Focused Ion Beam (FIB): a novel technology for advanced application of micro- and nanoanalysis in geosciences and applied mineralogy. European Journal of Mineralogy 16, 863–877.
Wirth, R., 2009. Focused Ion Beam (FIB) combined with SEM and TEM: advanced analytical tools for studies of chemical composition, microstructure and crystal structure in geomaterials on a nanometer scale. Chemical Geology 261, 217–229.
Young, R.J., 1997. Application of the focused ion beam in materials characterization and failure analysis. Microstructural Science 25, 491–496.